Mineralium Deposita
https://doi.org/10.1007/s00126-024-01259-2

ARTICLE

Sodic-calcic alteration and transpressional shear along the Atacama fault system during IOCG mineralization, Copiapó, Chile

N. M. Seymour[1,2,3] · J. S. Singleton[1] · R. Gomila[4,5] · G. Arancibia[4] · J. Ridley[1] · M. L. Gevedon[6] · D. F. Stockli[7] · S. M. Seman[7]

Received: 26 June 2023 / Accepted: 8 March 2024

Abstract

The Punta del Cobre district near Copiapó is a center of iron oxide-copper–gold (IOCG) mineralization spatially and temporally associated with regional sodic-calcic hydrothermal alteration, the Atacama fault system (AFS), and two phases of Early Cretaceous magmatism. Here, we investigate the spatiotemporal and geochemical relationships between magmatism, ductile deformation, and hydrothermal alteration along the ~ 200 to 300-m-thick steeply NW-dipping Sierra Chicharra shear zone, interpreted to be the major strand of the AFS. Mylonitic fabrics and oblique sinistral-reverse kinematic indicators together record coaxial flattening in a transpressional regime. Deformation on the AFS took place before, during, and after intrusion of the synkinematic Sierra Chicharra quartz diorite of the Coastal Cordillera arc at ~ 122 Ma and terminated before intrusion of the unstrained ~ 114 Ma Sierra Atacama diorite of the Copiapó batholith. Geochemical data show that the Copiapó batholith was more mafic and more K-rich than the calc-alkaline Coastal Cordillera arc. This time period thus overlaps IOCG mineralization in the Punta del Cobre district (~ 120 to 110 Ma). Multiple phases of sodic-calcic alteration in and around the AFS shear zone are recognized. Textures of altered rock in the shear zone show both synkinematic assemblages and post-kinematic hydrothermal oligoclase. A ~ 775-m-long andradite vein that cuts the shear zone formed broadly at the end of magmatism in the district (~ 95 Ma). Oxygen isotope ratios from the vein indicate that hydrothermal fluids were likely magmatically derived. Together, this work shows the AFS-related shear zone and nearby IOCG mineralization developed in a regional transpressional regime produced by SE-directed oblique convergence across a NE-striking shear zone. IOCG-related magmatic-hydrothermal fluids exploited this transcrustal shear zone to produce multiple episodes of regional sodic-calcic alteration formed from fluids exsolved from magmas or driven by the heat of the Coastal Cordillera arc and Copiapó batholith.

Keywords Atacama fault system · Coastal Cordillera arc · Copiapó batholith · Chilean Iron Belt · Punta del Cobre district

Introduction

The Jurassic to Early Cretaceous Coastal Cordillera arc of northern Chile and southern Peru is a host for multiple hydrothermal iron oxide-copper–gold (IOCG) ores

Editorial handling: N. F. Jansson

✉ N. M. Seymour
nseymour@oxy.edu

[1] Department of Geosciences, Colorado State University, 1482 Campus Delivery, Fort Collins, CO 80523, USA

[2] Department of Earth and Planetary Sciences, Stanford University, 450 Jane Stanford Way, Stanford, CA 94305, USA

[3] Department of Geology, Occidental College, 1600 Campus Drive, Los Angeles, CA 90042, USA

[4] Departamento de Ingeniería Estructural y Geotécnica, Pontificia Universidad Católica de Chile, Santiago, Chile

[5] Dipartimento Di Geoscienze, Università Degli Studi Di Padova, Padua, Italy

[6] Department of Geology, Colorado College, 14 E. Cache La Poudre, CO Springs, CO 80903, USA

[7] Department of Earth and Planetary Sciences, The University of Texas at Austin, 2305 Speedway Stop C1160, Austin, TX 78712, USA

Published online: 09 April 2024

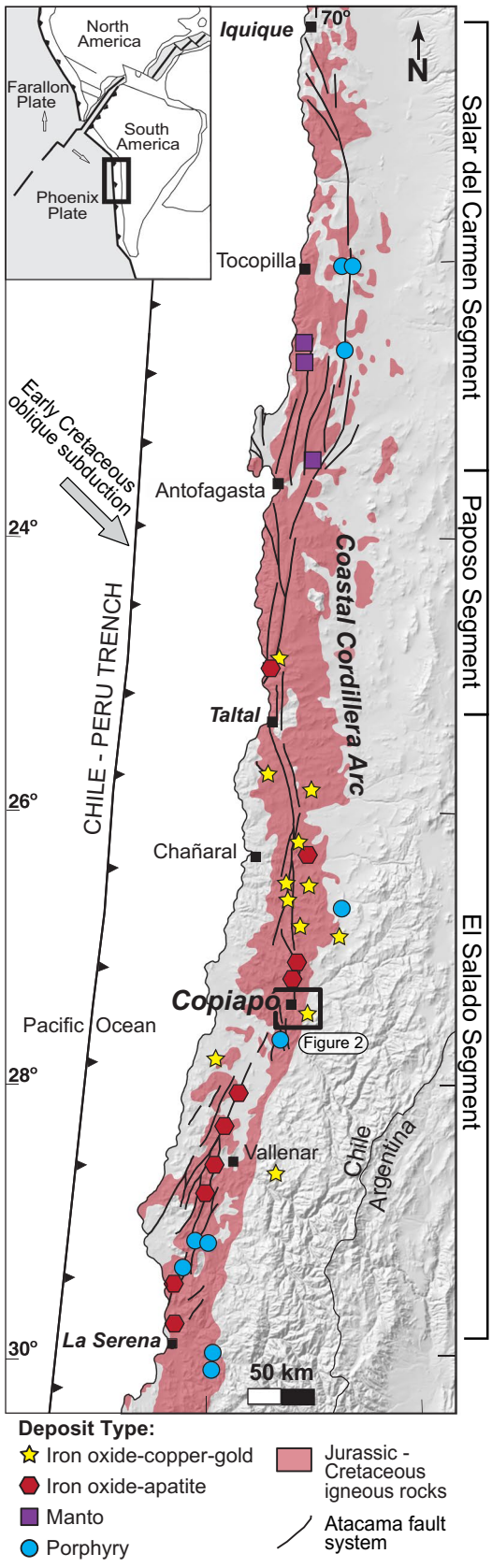

Fig. 1 Modern-day topography of northern Chile overlain with distribution of Jurassic-Cretaceous igneous rocks of the Coastal Cordillera arc from SERNAGEOMIN regional quadrangles, the regional geometry of the three major segments of the crustal-scale Atacama fault system (AFS) adapted from Cembrano et al. (2005), and ore deposit locations from Sillitoe (2003), Barra et al. (2017), and Salazar et al. (2020). Note the strong spatial correlation between the Coastal Cordillera arc, AFS, and economic deposits. Approximate Mesozoic oblique convergence vector from Jaillard et al. (1990) is indicated by the gray arrow. Location of Fig. 2 is shown by the black box. Inset map shows the Mesozoic plate tectonic configuration from Jaillard et al. (1990)

together with iron oxide-apatite (IOA) ores, formed along much of the length and over much of the history of the arc (Fig. 1) (e.g., Espinoza 1990; Vila et al. 1996; Marschik and Fontboté 2001a; Arévalo et al. 2006; Cembrano et al. 2009; Marquardt et al. 2009; Rieger et al. 2010; del Real et al. 2018; Simon et al. 2018; Palma et al. 2020; Salazar et al. 2020; Tornos et al. 2020). The arc, in contrast, hosts few porphyry deposits (Creixell et al. 2020; Rodriguez-Mustafa et al. 2020). Sillitoe (2003), Richards et al. (2017), and Skirrow (2022) suggest large-scale shifts in plate velocity and convergence angle resulted in a period of extension through the magmatic arc, reducing magmatic sulfur content in middle and upper crustal magma chambers and facilitating the development of IOCGs over porphyries. Extension is marked on a regional scale by development of back-arc basins filled with interbedded volcano-sedimentary and marine strata. The exact period of extension is, however, imperfectly constrained and may have been diachronous along the arc (e.g., Chen et al. 2013; Richards et al. 2017). Recent district-scale (up to 10 km) structural analysis by del Real et al. (2018; 2023) documents a shift from extensional back-arc basin sedimentation to syn-mineralization transpressional deformation around the IOCG deposits near Candelaria in northern Chile.

The proposed link between extension and IOCG deposits is also not supported by the kinematics of the Atacama fault system (AFS), which serves as an important control on the structural development of the Coastal Cordillera arc and on the location and style of associated mineralization (e.g., Sillitoe 2003; Arévalo and Creixell 2009; Cembrano et al. 2009; Marquardt et al. 2009). The AFS is a major (~ 1000 km long) system of N-striking fault branches and NNW- and WNW-striking second-order faults that formed within the Early Cretaceous arc between ~ 20.5° S and 30° S (Fig. 1) (Grocott et al. 1994; Wilson and Grocott 1999; Grocott and Taylor 2002). Kinematics along the main AFS branches are dominantly sinistral strike-slip and do not record a significant component of extension between 135 and 110 Ma (Seymour et al. 2020, 2021). Ruthven et al. (2019) document Early Cretaceous transpression along the southern

Paposo segment where the Paposo fault strikes ~ 020° and dips steeply east. In contrast, Cembrano et al. (2005) and Veloso et al. (2015) document transtension along the northern end of the Paposo segment, where major faults strike NNW to NW. Along much of the northern and the central El Salado segment north of Copiapó, the dominant trend of the AFS is ~ N-S and sinistral shear dominates and with no evidence for widespread transpression nor transtension (Seymour et al. 2021).

Arc intrusions played a fundamental role in controlling fault system behavior and localizing margin-parallel motion along the AFS. Mylonitic zones are localized within and adjacent to Early Cretaceous plutons and overprinted by brittle faults that indicate progressive ductile to brittle deformation as plutons intruded and subsequently cooled (Seymour et al. 2020). Cessation of movement along the AFS is interpreted to correlate with waning arc magmatism in the Coastal Cordillera and possibly a change in convergence vector from SW-directed oblique motion to arc perpendicular (Matthews et al. 2012). The change in plate motion was coeval with the onset of E-W tectonic shortening in the upper crust and eastward migration of magmatic centers (e.g., Mpodozis and Allmendinger 1993; Scheuber et al. 1994; Maksaev et al. 2009; Mavor et al. 2020).

The Punta del Cobre district, which lies ~ 17 to 23 km east of the AFS and along the eastern margin of the Copiapó batholith (Fig. 2) (Arévalo et al. 2006), contains the most significant cluster of actively mined IOCG deposits along the Peru–Chile margin including the Candelaria-Punta del Cobre deposit (del Real et al. 2023). The IOCG deposits in and around the Coastal Cordillera arc are invariably associated with regional voluminous sodic-calcic or sodic alteration, which is developed in both the plutons and overlying volcanic and sedimentary rocks (Barton et al. 2011; Barton 2014; del Real et al. 2018), similar to ores elsewhere in the world (Haynes 2000; Barton et al. 2013). However, the mineralized cores of the deposits are more typically characterized by potassic alteration assemblages, making a direct relationship between sodic-calcic and sodic alteration and ore precipitation unclear. Rieger et al. (2012), for instance, proposed that the fluid responsible for the sodic-calcic alteration acted as a dilutant and coolant to promote precipitation of IOCG ore from magmatic-hydrothermal fluids.

Here, we provide a detailed investigation of a ductile shear zone that is mapped as the main branch of the El Salado segment of the AFS (Arévalo 2005a) and has been overprinted by sodic-calcic alteration adjacent to the major field of IOCG deposits of the Punta del Cobre district around Copiapó. The shear zone developed between plutons of the Coastal Cordillera arc and Copiapó batholith (Arévalo 2005a). We incorporate geologic mapping, alteration and microstructural petrography, geochronology, and geochemistry to determine (1) the geometry, kinematics, and timing of mylonitic deformation along the AFS and (2) the spatiotemporal and geochemical relationships between IOCG mineralization, ductile deformation, hydrothermal alteration, and magmatism of both the Coastal Cordillera arc and Copiapó batholith. This investigation directly tests proposed links between IOCG mineralization and tectonic environment (Sillitoe 2003; Chen et al. 2013; Richards et al. 2017). In particular, we examine how the transition from Coastal Cordillera arc magmatism to Copiapó batholith emplacement and associated IOCG mineralization is related to the geometry and timing of deformation on the sinistral AFS. We focus on the nature, timing, and context of sodic-calcic alteration and related andradite-rich veins in the shear zone and compare our findings to the Punta del Cobre mining district to evaluate how alteration relates to regional spatial and temporal patterns of Coastal Cordillera arc magmatism, IOCG mineralization, and AFS deformation.

Geologic background

Tectonic framework of the Mesozoic Peru–Chile margin

Subduction along the Peru–Chile margin, the type locality of Andean-type ocean-continent subduction, has been ongoing since the Late Triassic and persists to the present day (Coira et al. 1982; Mpodozis and Ramos 1990; Mpodozis and Kay 1992; Parada et al. 2007; Ramos and Folguera 2009). Magmatism associated with subduction began as early as ~ 215 to 210 Ma (Rodríguez et al. 2019; Jara et al. 2021a) and migrated eastward in punctuated phases to the position of the modern-day Andean arc (Dallmeyer et al. 1996; Parada et al. 2007). Relative plate motion across the long-lived margin has varied through time as microplates were developed and consumed and global tectonic reorganizations occurred (Seton et al. 2012; Matthews et al. 2012; Butterworth et al. 2016). The calc-alkaline Mesozoic Coastal Cordillera arc and related back-arc basin deposits now exposed along the northern Chilean coast developed above an obliquely convergent margin as the Phoenix (Aluk) plate subducted southeastward below the N-S trending margin of Gondwana (Fig. 1) (Coira et al. 1982). Plutons in this region intruded the middle to shallow crust (< 10 km depth) in Early Jurassic (195–175 Ma), latest Jurassic to Early Cretaceous (150–120 Ma), and late Aptian to early Cenomanian (120–99 Ma) pulses (Naranjo et al. 1984; Berg and Baumann 1985; Dallmeyer et al. 1996; Parada et al. 2007; Oliveros et al. 2010; Seymour et al. 2020; Jara et al. 2021a, 2021b). The first two pulses are related to the Coastal Cordillera arc, and the later phase reflects a transition to more localized post-arc magmatism.

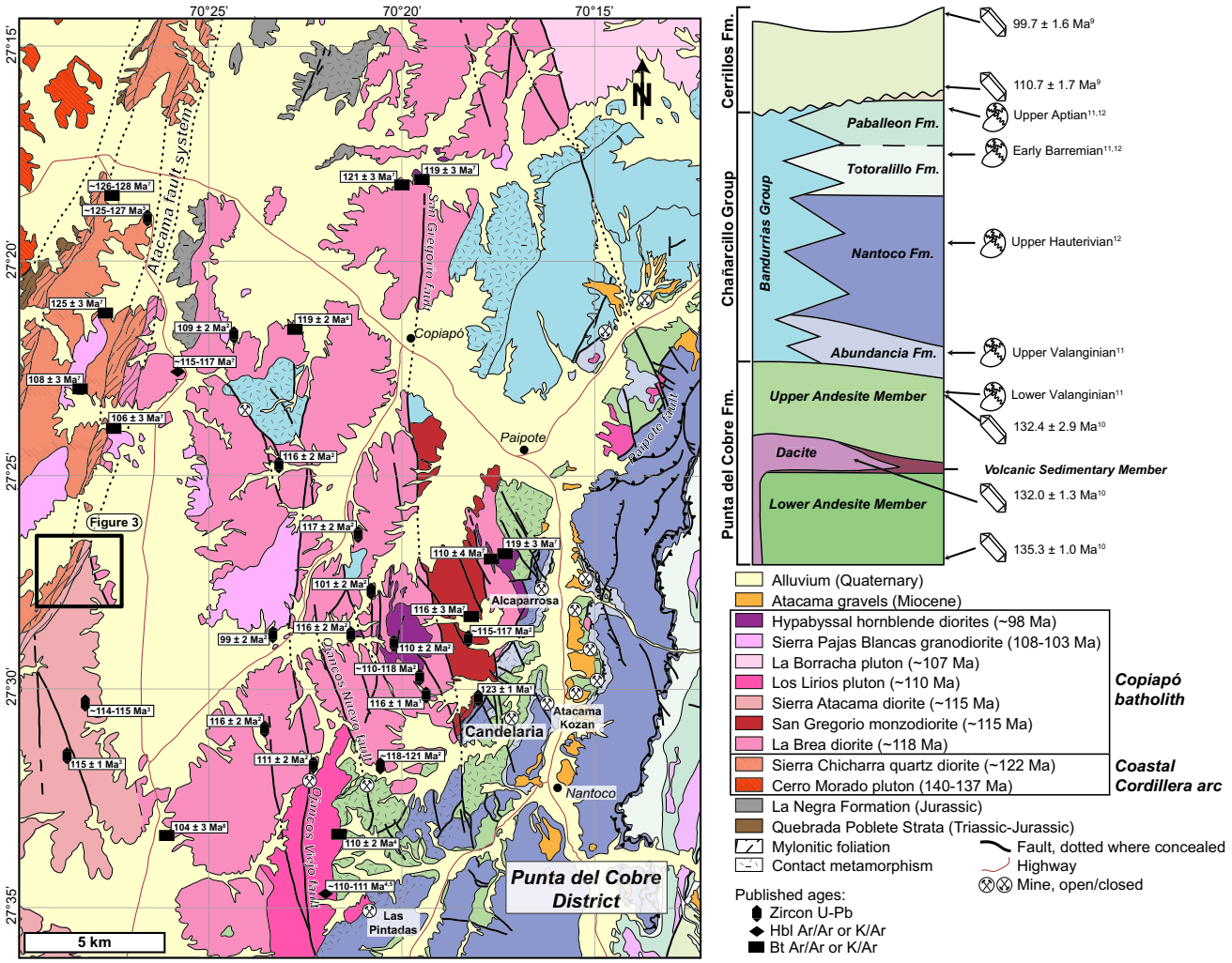

Fig. 2 Regional map of bedrock geology in the Copiapó region modified from Arévalo (2005a, 2005b). Coastal Cordillera arc plutons are located to the west (indicated by diagonal hatching), Copiapó batholith plutons through the center, and the Early Cretaceous sedimentary sequence to the east. Stratigraphy of the sedimentary sequence is modified from del Real et al. (2018). Major regional structures are labeled. Note that the Atacama fault system occurs through this region only as a ductile shear zone. Published age data are as follows: igneous zircon U–Pb from (1) Marschik and Sollner (2006), (2) Girardi (2014), and (3) Jara et al. (2021a); hornblende and biotite Ar/Ar from (4) Arevalo et al. (2006); hornblende and biotite K/Ar from (5) Arevalo (1994), (6) Arevalo (1995), (7) Arevalo (2005a), and (8) Arevalo et al. (2005b); detrital zircon U–Pb from (9) Maksaev et al. (2009) and (10) del Real et al. (2018); and ammonite stratigraphy from (11) Mourgues (2004) and (12) Aguirre-Urreta et al. (2007). The locations of Punta del Cobre district deposits from Sillitoe (2003) and Marschik and Söllner (2006) are shown with crossed hammers. Location of Fig. 3 is shown in the black box

Deformation along the intra-arc AFS is related to the oblique component of plate convergence. The AFS is subdivided into three major segments: the northern Salar del Carmen, central Paposo, and southern El Salado segments (Fig. 1). Thermal weakening associated with the intrusion of arc plutons facilitated sinistral motion (e.g., Seymour et al. 2020). Kinematically compatible brittle faults overprint mylonitic fabrics along the Paposo and El Salado segments (Brown et al. 1993; Scheuber and Gonzalez 1999; Grocott and Taylor 2002). Overprinting relationships record a progressive transition from sinistral strike-slip ductile shear, which initiated with the shallow (< 10 km) emplacement of Early Cretaceous plutons, to sinistral brittle strike-slip deformation (Scheuber et al. 1995; Dallmeyer et al. 1996; Ruthven et al. 2019). The transition to brittle deformation occurred as magmatism migrated eastward and elevated thermal gradients in the arc region relaxed (Scheuber et al. 1994; Seymour et al. 2020).

Geology of the Copiapó region

The El Salado segment of the AFS is exposed for ~ 480 km between the cities of Taltal (25.4° S) and La Serena (30° S) (Fig. 1). Fault orientation changes from dominantly

N-S-striking multi-strand fault branches between Taltal and Copiapó to an overstepping set of NE-striking faults between Copiapó and La Serena. Where the orientation of the fault system segment shifts from N-striking to NE-striking near the city of Copiapó, brittle faults are not recognized. Instead, the AFS is mapped at 1:100,000 scale as a subvertical 300–600-m-wide NNE-striking ductile shear zone, herein called the Sierra Chicharra shear zone (Arévalo 2005a) (Fig. 2).

Oblique convergence that produced sinistral slip along the AFS transitioned to E-W shortening in the late Early Cretaceous (Scheuber et al. 1994). Shortening was accommodated within the Punta del Cobre district by the W-vergent Paipote thrust fault, NNE-trending upright Tierra Amarillo anticlinorium, and N- to NW-striking, steeply dipping faults that cut both the Copiapó batholith and overlying sedimentary section (Arévalo 2005a, b; Maksaev et al. 2009; Martínez et al. 2013; del Real et al. 2018, 2023). Displacement on these structures ranges from 10 s of meters to 1 km of dip-slip motion (Arévalo et al. 2006; Kreiner 2011) and may have accommodated horizontal as well as vertical motion (del Real et al. 2023). The ages given for the change of structural regime are not consistent: at a plate-margin scale, Chen et al. (2013) suggest a shift at 120 to 100 Ma based on plate reconfiguration. Near Copiapó, Maksaev et al. (2009) state that extension continues up to ~ 111 Ma based on the age of the continental lower Cerrillos Formation. However, other authors indicate that inversion of the Chañarcillo basin occurred between ~ 115 and 110 Ma, as recorded by a regional angular unconformity between the tilted Valanginian to Aptian Chañarcillo and Bandurrias Groups and overlying Albian Cerrillos Formation (Fig. 2) (Amilibia 2009; del Real et al. 2018).

Compiled published data record a broad magmatic peak in the Copiapó area between ~ 140 and 100 Ma, corresponding primarily to the plutonic rocks of the Coastal Cordillera arc, including the Cerro Morado (140–137 Ma), La Brea (123–117 Ma), and La Borracha (~ 107 Ma) plutons (Farrar et al. 1970; Arévalo 1995, 1999; Ullrich et al. 2001; Girardi 2014). The second major phase and focus of magmatism in the area, which both overlaps and postdates the cessation of Coastal Cordillera arc magmatism, is represented by the mafic to intermediate Copiapó batholith (e.g., Marschik et al. 2003; Marschik and Söllner 2006). The multi-phase magmatism of the Copiapó batholith marks migration of the focus of magmatism ~ 15 km east from the main line of the Coastal Cordillera arc and the AFS (Fig. 2). The batholith was active between 120 and 110 Ma, with minor intrusive activity continuing to about 97 Ma (Marschik and Söllner 2006; Girardi 2014; del Real et al. 2023), and intruded back-arc marine sediments of the Valanginian to Aptian Punta del Cobre Formation, Chañarcillo Group, and Bandurrias Group. Major magma compositions include two-pyroxene diorites, monzodiorites, and tonalites (Arévalo 2005a) and include both calcic calc-alkaline and high-K calc-alkaline phases (Marschik et al. 2003).

Hydrothermal alteration and mineralization in the Punta del Cobre district

Alteration has been mapped throughout the Copiapó batholith by Kreiner (2011), Barton et al. (2013), and others. Studies on individual deposits in the Punta del Cobre district have focused on the extent and style of hydrothermal alteration and mineralizing processes including the timing and style of mineralization and composition and source of mineralizing fluids (Barton and Johnson 1996; Marschik and Fontboté 2001a; Mathur et al. 2002; Sillitoe 2003; Gelcich et al. 2005; Tornos et al. 2010; Daroch and Barton 2011; Rieger et al. 2012; Lopez et al. 2014; Marschik and Kendrick 2015; Veloso et al. 2017; del Real et al. 2018). Despite this large body of work and the concentration of ores near the margins of phases of the batholith, direct links between phases of mineralization, alteration, and causative intrusions have not been clearly established (Barton and Johnson 2000; Marschik and Fontboté 2001a; Mathur et al. 2002; Barton et al. 2005; Arévalo et al. 2006; Chiaradia et al. 2006).

District-scale alteration is characterized by sodic- and sodic-calcic assemblages of oligoclase and actinolite with accessory titanite, rutile, apatite, and clinopyroxene (Barton et al. 2011), especially in the northwestern portion of the Punta del Cobre district (del Real et al. 2018). This zone is located within the thermal aureole of Copiapó batholith plutons (Zentilli 1974; Marschik et al. 1997; Ullrich and Clark 1998; Marschik and Fontbote 2001a; Ullrich et al. 2001; Mathur et al. 2002; Arévalo 2005a, b; Arévalo et al. 2006; Kreiner 2011). More localized alteration zones characterized by potassium feldspar, biotite, actinolite, magnetite, and chalcopyrite are associated with main-stage Cu mineralization hosted along the contact between the lower andesite and volcanic-sedimentary/dacite units of the Punta del Cobre Formation (Marschik and Fontboté 2001b; del Real et al. 2018) (Fig. 2). Quartz and epidote are uncommon in alteration assemblages.

IOCG ore consists mainly of magnetite, chalcopyrite, and pyrite associated with actinolite, biotite, and chlorite (Ryan et al. 1995) and occasionally includes andradite-bearing assemblages such as those found at Alcaparrosa, Atacama Kozan, and Candelaria. Las Pintadas, a classic calcic skarn hosted in the Chañarcillo Formation at the La Farola deposit, also hosts abundant garnet (Marschik and Fontboté 2001b; del Real et al. 2018). Ore occurs either as disseminated, patchy sulfide mineralization hosted by stratigraphically controlled mantos, within breccia-hosted ore bodies, or as veins along steeply dipping brittle faults that grade downward into shear zones in the batholith and supracrustal

rocks (Camus 1980; Ryan et al. 1995; Marschik and Fontboté 2001a). Ore textures, including deformed, foliation-parallel sulfide horizons in the low-angle Ojancos shear zone at Candelaria Norte and undeformed sulfide-hematite veins cutting the foliated Ojancos shear zone fabrics, suggest mineralization occurred during the transition from ductile to brittle deformation in a cooling hydrothermal system (del Real et al. 2018).

Regional sodic-calcic alteration has not been dated, though cross-cutting relationships in the Punta del Cobre district suggest that it may be as early as 120 Ma (del Real et al. 2018). $^{40}Ar/^{39}Ar$ dates on hydrothermal biotite at Candelaria record local potassic alteration between 116 and 110 Ma (Ullrich and Clark 1998, 1999; Marschik and Fontboté 2001a). Three generations of mineralized vein systems have been documented in the Copiapó region which may be related to either the main or late stage of mineralization: (1) a minor early stage hosted by the Early Cretaceous volcanic-sedimentary sequence and cut by ~ 127 Ma dikes (Kreiner 2011), (2) a main stage related to emplacement of La Brea diorite at ~ 117 Ma (Kreiner 2011), and (3) a late stage at ~ 115 Ma contemporaneous with nearby Copiapó batholith emplacement (Zentilli 1974; Marschik et al. 1997; Ullrich and Clark 1998). Of these, the ~ 115 Ma pulse is the economically most important. Re-Os dates on molybdenite record Cu-Au mineralization at 115.2 to 114.2 Ma at Candelaria (Mathur et al. 2002).

Methods

Field investigations

We investigated a ~ 6 km^2 area centered on a ductile shear zone previously mapped as the main branch of the AFS, referred to as the Sierra Chicharra shear zone in this study. The shear zone is located ~ 17 km SW of Copiapó and ~ 20 km WNW of the Punta del Cobre district and Candelaria deposit (black box in Fig. 2). Previous bedrock mapping was conducted at 1:100,000 scale by Arévalo (1994, 1995, 2005a, b). We conducted 1:10,000-scale field mapping (Fig. 3, Supplementary Fig. 1) to determine kinematics of the shear zone and resolve relationships between alteration in the Sierra Chicharra shear zone and local plutons.

We documented lithologies, geometry and intensity of fabrics, cross-cutting relationships, and the nature and distribution of alteration. Structures were measured with a Brunton compass, and average orientations were determined using maximum eigenvectors in the Stereonet© software (Allmendinger et al. 2011; Cardozo and Allmendinger 2013). Shear sense indicators including asymmetric porphyroclasts, asymmetric folds, and shear bands were used to determine the kinematics of macroscopic or mesoscale mylonitic fabrics. We collected oriented samples for thin section petrography and microstructural analysis and bulk samples for geochronologic and geochemical analyses from syn- and post-kinematic plutons. Oriented samples were cut parallel to lineation and perpendicular to foliation. We applied whole-rock geochemistry to investigate the association of the plutons and the chemical nature of alteration.

U–Pb geochronology

Zircon and garnet were analyzed for U–Pb geochronology by laser ablation inductively coupled-plasma mass spectrometry to determine the timing of pluton intrusion and hydrothermal vein formation. We also attempted to analyze titanite to directly date alteration; however, reconnaissance analyses revealed that the titanite did not have sufficient [U] to produce robust geochronologic data. Euhedral, unpolished zircons from samples 161–2, 161–9, and 191-N116 were mounted parallel to the c-axis on double-sided tape for depth profiling to capture any potential core-and-rim relationships (e.g., Coastal Cordillera plutons documented in Seymour et al. (2020, 2021)). Following depth profile analysis, additional zircons from 161–9 and 191-N116 were mounted in epoxy, polished to expose the center of the grains, and imaged using cathodoluminescence (CL) to document internal zoning patterns and better understand the source of complexity in the single-grain zircon U–Pb data (Supplementary Fig. 2). Euhedral garnet crystals were picked out of vein hand samples, mounted in epoxy, and polished. Garnet fragments were analyzed with energy dispersive spectroscopy on a Philips/FEI XL30 environmental scanning electron microscope to identify andradite-rich growth domains to target for U–Pb analysis (Gevedon et al. 2018).

Prepared samples were ablated with a PhotonMachine Analyte G.2 excimer laser in the UTChron Laboratories at the University of Texas at Austin. Approximately 30 zircon grains per sample were ablated using a 30-µm-diameter spot with a repetition rate of 10 Hz for 30 s at 100% laser power. Pit depths were ~ 17 µm. Garnet fragments were analyzed using the methods of Seman et al. (2017). Approximately 50 garnet sites were ablated using a 110-µm-diameter spot with a repetition rate of 10 Hz for 30 s at 83% laser power. The larger spot size was used to maximize [U] liberated during ablation and minimize the effects of downhole fractionation.

Ablated material was analyzed on a Thermo Scientific Element 2 high-resolution magnetic sector inductively coupled plasma mass spectrometer (ICP-MS). Zircon analyses were interspersed 5:1 with primary standard GJ1 (608.53 ± 0.37 Ma) (Jackson et al. 2004) to correct for instrument drift as well as elemental and downhole fractionation. Secondary standards Pak1 (43.03 ± 0.01 Ma

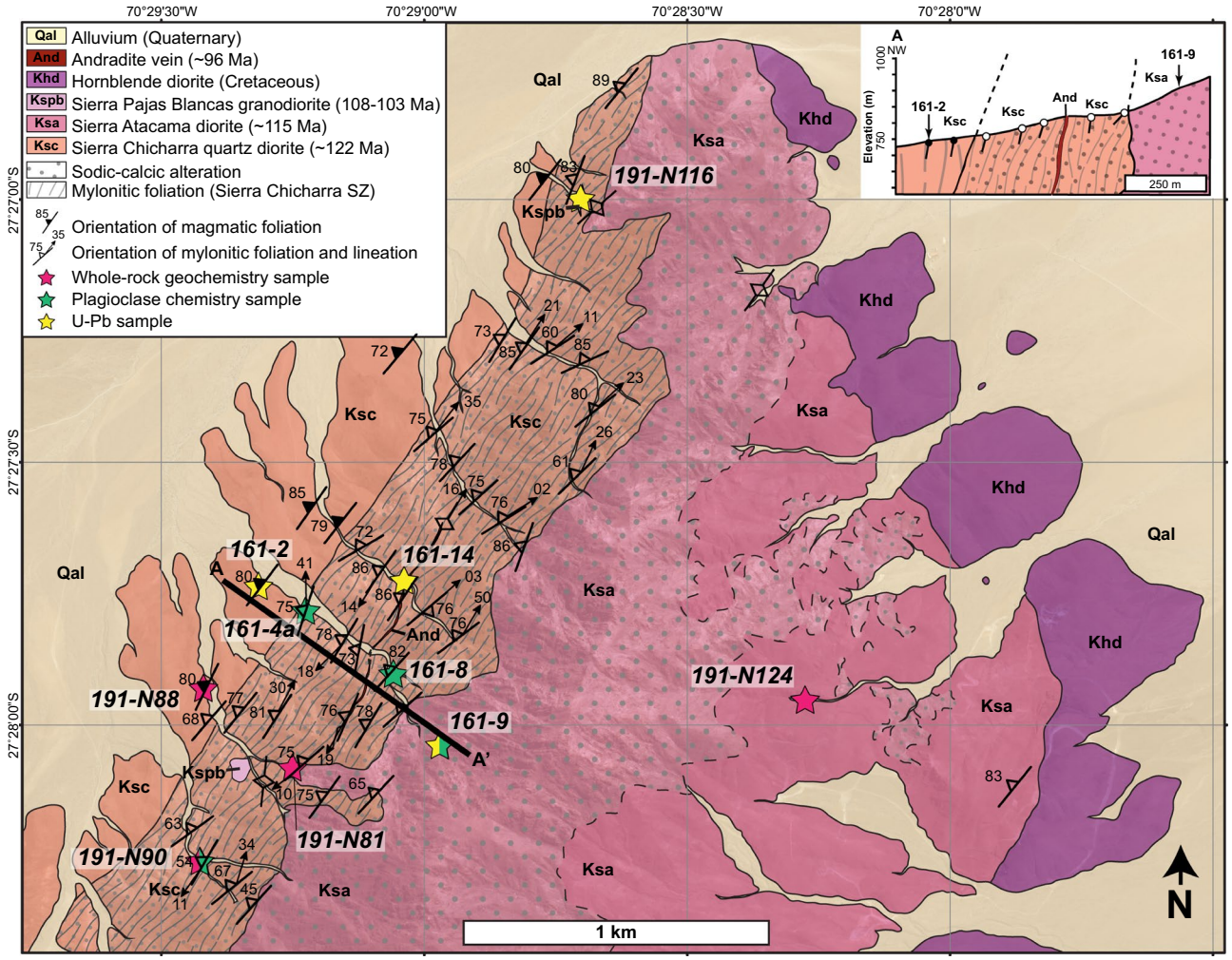

Fig. 3 Detailed mapping of the ductile Sierra Chicharra shear zone. Locations of samples analyzed for whole-rock geochemistry, plagioclase mineral chemistry, and U–Pb geochronology are shown. Inset shows cross-section A-A′ through the shear zone. See Supplementary Fig. 1 for 1:10,000-scale version of this map, which includes additional structural measurements at a finer scale

TIMS, in-house standard) and Plesovice (337.13 ± 0.37 Ma TIMS) (Slama et al. 2008) were interspersed 1:15 with unknowns to monitor data quality and date accuracy. Garnet analyses were interspersed 5:1 with primary standard Willsboro andradite (1022 ± 16 Ma TIMS) (Seman et al. 2017) and 15:1 with secondary standards Mali grandite (202.0 ± 1.2 Ma TIMS) (Seman et al. 2017), Lake Jaco grossular (34.0 ± 1.4 Ma LA-ICP-MS) (Seman et al. 2017), and zircon standard GJ1 (608.53 ± 0.37 Ma) (Jackson et al. 2004).

Raw isotopic ratios were reduced in iolite using VizualAgeDRS and plotted with IsoplotR (Paton et al. 2011; Petrus and Kamber 2012; Vermeesch 2018). The U decay constant of Jaffey et al. (1971) was used for all date calculations. The uncertainty reported for individual grains represents the combined internal and external error. $^{206}Pb/^{238}U$ dates are reported for all zircon grains. Reduced single-grain data with $^{206}Pb/^{238}U$ dates and $^{207}Pb/^{235}U$ dates that differed by < 10% (i.e., discordance) were filtered out to eliminate grains with significant Pb loss. Zircon crystallization age spectra are complex and are discussed in detail below. Garnet dates were plotted in Tera-Wasserburg space, and the lower $^{238}U/^{206}Pb$ intercept is interpreted to represent the crystallization age.

Whole-rock and plagioclase geochemistry

We compiled geochemical data for the area shown in Fig. 2 from published studies to evaluate the igneous signatures of the Coastal Cordillera and Copiapó batholith as well as major element shifts resulting from alteration. Four newly collected bulk geochemical samples from units across the study area (samples 191-N88, 191-N81, 191-N90, and 191-N124) were pulverized and sent to

Activation Laboratories Ltd. for major and trace element whole-rock geochemistry. Sample powders were subjected to a four-acid leach according to the 4E-Exploration analytical package and analyzed by inductively coupled plasma mass spectrometry. Values are reported as weight percent oxides for major elements and parts per million (ppm) for trace elements.

To tie whole-rock data to petrographic textures, we analyzed the composition of primary and secondary plagioclase both within the shear zone and the variably altered Sierra Atacama pluton. Plagioclase from 4 samples (161-4a, 161–8, 191-N90, and 161–9) was analyzed using a JEOL JXA-8230 SuperProbe electron microprobe (EPMA) equipped with 5 wavelength-dispersive X-ray spectrometers (WDS) at the Mineral and Microchemical Analysis Facility, Stanford University. Polished thin sections were carbon coated to ~ 15 nm to prevent the effects of charging under the electron beam. In situ plagioclase crystals were analyzed with 15 kV accelerating voltage, 20 nA beam current, and 10 µm beam diameter to mitigate alkali migration and volatilization. Analyses were standardized on a natural labradorite (NMNH 115900) and natural Amelia albite (C.M. Taylor collection).

Oxygen isotope ratios

We analyzed quartz, epidote, and garnet from the hydrothermal andradite vein (sample 161–14) to determine the composition and source of alteration-related hydrothermal fluids. Silicate mineral separates from one sample were washed in dilute HCl to remove carbonate, rinsed in deionized water, and handpicked under a binocular microscope to avoid pieces with visible mineral inclusions. Magnetite and mineral fragments with magnetite inclusions were removed with a hand magnet. Approximately 2.0 mg of mineral separates was analyzed on a laser fluorination extraction line using BrF_5, coupled with a Thermo MAT253 stable isotope ratio mass spectrometer at the Light Isotope Laboratory at the University of Texas at Austin according to the methods presented in Sharp (1990). Garnet and quartz standards UWG-2 ($\delta^{18}O + 5.8‰$) (Valley et al. 1995) and Lausanne-1 ($\delta^{18}O + 18.1‰$; in-house standard) were run as a part of the analytical session to track precision and accuracy of measurements. Analytical error is ± 0.1‰, and isotopic values are reported relative to Vienna Standard Mean Ocean Water (VSMOW).

Results

Map relationships

We present cross-cutting relationships beginning with exposures west of the Sierra Chicharra shear zone and moving east (Fig. 3). The western side consists entirely of a medium-grained mesocratic biotite quartz diorite mapped by Arévalo (2005a, b) as the Sierra Chicharra pluton. Outcrops are recessive, and the pluton is weathered to grus (Fig. 4a). Magmatic foliation defined by aligned biotite dips steeply NW and is pervasive throughout the exposure of the pluton. Near the margin of the shear zone, the magmatic fabric transitions to a zone of protomylonitic and mylonitic fabrics. The transition to solid-state fabrics correlates with the edge of a bleached zone of plagioclase-actinolite alteration trending ~ 212°.

Pinstripe ultramylonites with well-developed cm- to mm-scale, steeply NW-dipping banding characterize the ~ 200 to 300-m-wide Sierra Chicharra shear zone (Fig. 4b). Mylonitic fabrics have a strong foliation defined by green and white bands and locally have a mineral lineation defined by aligned amphiboles. These fabrics are cut by a small stock of unstrained and unaltered medium-grained hornblende granodiorite and a ~ 1-m-wide hornblende granodiorite dike (Fig. 4c). Near the center of the shear zone, a ~ 2–3-m-wide andradite-rich vein extends ~ 775 m along a NNE-SSW (~ 023°) trend (Fig. 3). A magnetite-rich zone of this vein has been prospected but is not being actively worked. Massive garnet is often associated with classic calcic skarns; however, there is no evidence of a carbonate host rock within the study area, and this feature is thus interpreted as a hydrothermal vein. The margins of the vein are relatively sharp and lined with massive brown garnet (Fig. 4e). There is a narrow bleached ~ 1- to 2-mm-wide contact zone in the wallrock.

The eastern shear zone margin is irregularly cut by an altered, internally unstrained pluton (Fig. 4d). This pluton is mapped as the Sierra Atacama diorite by Arévalo (2005a, b). Pervasive alteration typically extends about 1 km east of the intrusive contact with the shear zone. The unaltered pluton is a mesocratic medium-grained hornblende diorite. The contact between altered and unaltered pluton is both irregular and gradational at the meter scale (Fig. 3). A medium- to coarse-grained melanocratic hornblende diorite intrudes both the altered rocks of the Sierra Chicharra shear zone and the bleached Sierra Atacama diorite at the northern end of the study area and continues to the southeast along a line of mine workings associated with the Andacollita mine (Fig. 3). Locally, it is difficult to distinguish the hornblende diorite from the Sierra Atacama diorite due to the similarity of the color index and mineralogy.

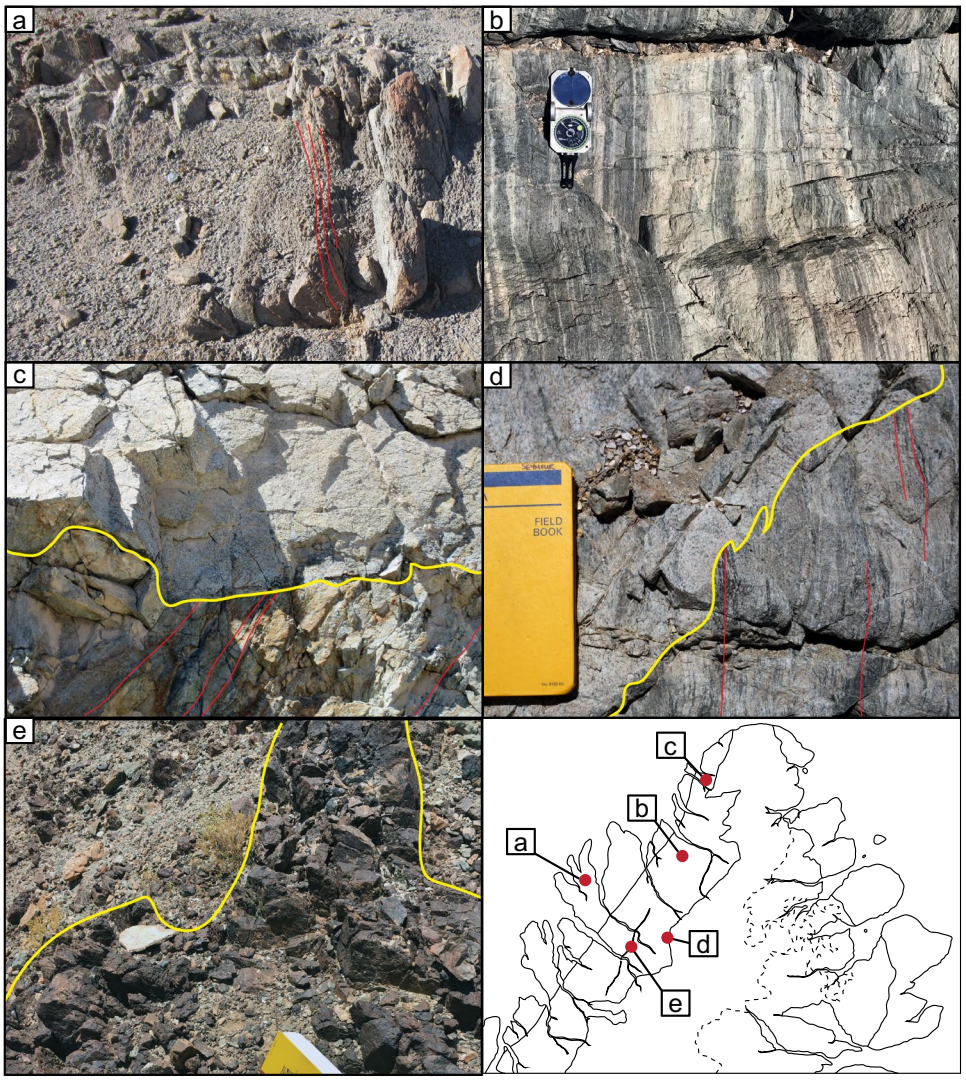

Fig. 4 Field photographs of **a** magmatic foliation (marked by red lines) and grus-type weathering in the Sierra Chicharra quartz diorite west of the Sierra Chicharra shear zone, **b** "pinstripe" green-and-white hydrothermally altered mylonitic shear zone defining the AFS, **c** hornblende diorite dike cutting mylonitic fabrics and alteration within the shear zone, **d** unstrained but bleached Sierra Atacama diorite cross-cutting the mylonitic fabrics of the shear zone, and **e** andradite vein cross-cutting the shear zone. In all photos, contacts are marked by yellow lines and mylonitic foliations are marked by red lines. Lower right panel shows a simplified version of Fig. 3 an index map for field photograph locations

Kinematics of ductile fabrics in the Sierra Chicharra shear zone

Ductile kinematic indicators record sinistral shear as well as apparent W-side-up reverse motion. On surfaces that are parallel to lineations and perpendicular to foliation, φ-clasts and the symmetric warping of foliation around boudinaged layers record a high degree of coaxial shortening normal to the shear zone boundary (Fig. 5a). Where clear shear sense indicators such as sigmoidal foliation patterns and C′ shear bands are present, sinistral shear sense indicators dominate. Subvertical exposures at a high angle to lineations locally show late-stage W-side-up reverse-sense shear bands (Fig. 5b). Near the center of the ~ 200- to 300-m-wide Sierra Chicharra shear zone, discontinuous foliation-parallel breccia zones up to 10 cm wide locally overprint mylonites (Fig. 5c). A map-scale brittle fault is not present in this area at 1:10,000 scale.

Contacts between granitic rocks with magmatic fabrics (average orientation 219/79 W) and solid-state mylonitic foliations (average orientation 218/74 NW) are concordant and locally gradational (Fig. 5d). The average mylonitic and magmatic foliation and a slight majority of individual foliation orientations strike clockwise from the western margin of the shear zone boundary, which is consistent with a component of sinistral shear. We did not observe a systematic difference in foliation orientations between higher strain and lower strain domains. Mineral lineations were identified in about a third of outcrops and dominantly plunge < 45° to the NE ($n = 14/19$) with a smaller proportion plunging < 45° to the SW ($n = 5/19$). Lineations have an average orientation of 033/20 (Fig. 5d). The predominance of foliation development over lineation development classifies these fabrics as S- to S > L tectonites.

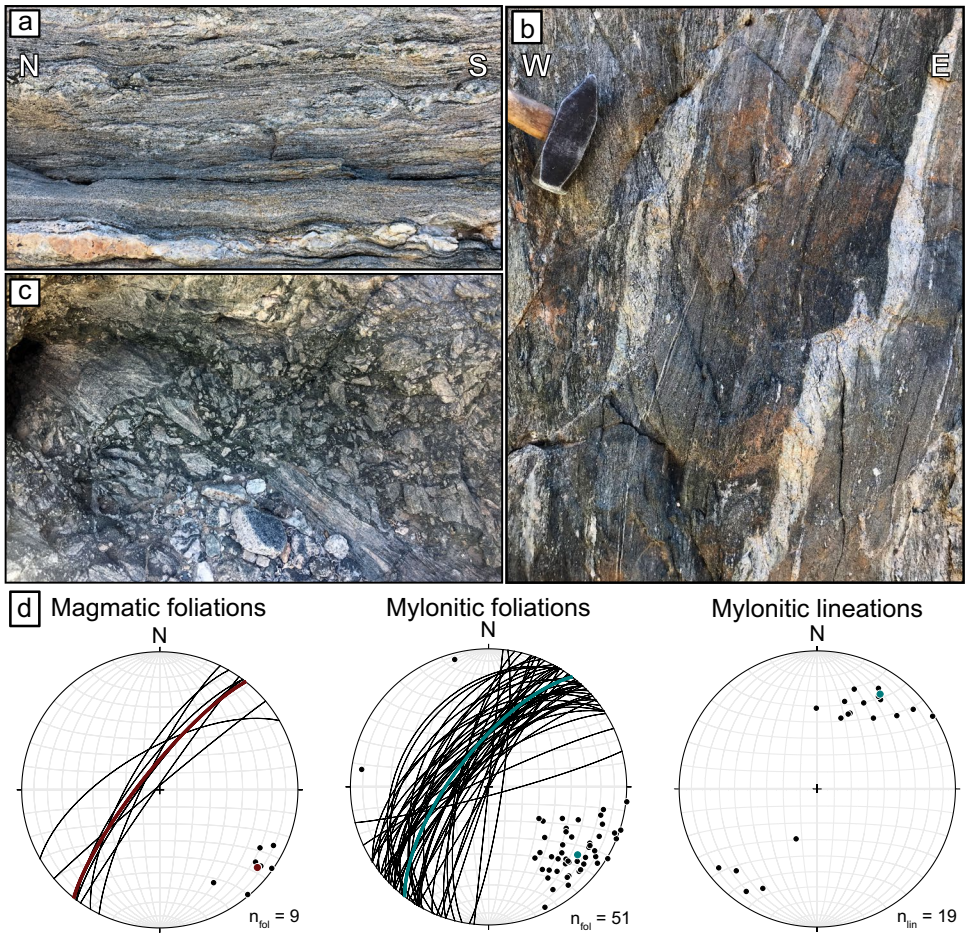

Fig. 5 Field photographs showing macroscopic mylonitic fabrics and shear sense indicators within the mylonitic Sierra Chicharra shear zone. **a** Top-down (lineation-parallel) view showing mylonitic fabrics with coaxial warping around boudins and sinistral asymmetric pods. **b** Lineation-perpendicular view showing late-stage, reverse-sense shear bands cutting compositional layering in macroscopically mylonitic fabrics. **c** Angular clasts of mylonitic rocks in a jigsaw-textured breccia with actinolite and epidote matrix. Foliation-parallel pockets of this breccia type are found within the shear zone. **d** Stereographs of planes and poles to the magmatic foliation within the Sierra Chicharra quartz diorite (left), planes and poles to the mylonitic foliation within the shear zone (middle), and mylonitic lineations in the shear zone (right)

Magmatic and alteration petrography

The Sierra Chicharra pluton is composed of 2- to 4-mm euhedral- to subhedral plagioclase (55–65%); 1 mm anhedral, unstrained quartz (10–15%); and subequal proportions of 0.5–1-mm brown biotite and green hornblende, locally with apatite inclusions. Primary rutile is not present. The pluton is generally unaltered except for minor development of epidote and fine-grained white mica in the cores of some plagioclase (Fig. 6a). Chlorite and titanite appear and become more common with increasing proximity to the shear zone, especially as magmatic fabrics defined by biotite transition to mylonitic fabrics.

Petrographic analysis reveals that mylonitic fabrics in the Sierra Chicharra shear zone are completely annealed (Fig. 6b–d). Green foliation planes are defined by aligned actinolite, epidote, and titanite. Locally, rutile mantled by elongate titanite is also present, and actinolite shows undulatory extinction. Plagioclase occurs as smaller crystals pinned between foliation planes where spacing is on the order of ~ 1 mm (Fig. 6b, d) or as coarse (3 to > 10 mm) blocky plagioclase grown around the mafic phases in a chessboard pattern in samples with closely spaced foliation (Fig. 6c). Igneous plagioclase textures such as oscillatory zoning and polysynthetic twinning are absent, and crystals are large (> 1 mm) compared to other phases (≤ 0.5 mm) (Fig. 6c). Samples with sub-cm- to mm-scale foliation planes hosted in larger, internally structureless feldspar are concentrated near the center of the shear zone. Breccias within the mylonite zone are composed of monomict angular clasts of the green-and-white banded sheared rock in a matrix of actinolite and epidote. Locally, the long axes of the actinolite and epidote in the breccia matrix are aligned, but neither the orientations of elongate minerals nor the long axes of clasts record a systematic preferred orientation.

The unaltered part of the Sierra Atacama pluton is a subhedral granular hornblende diorite composed of plagioclase, green hornblende, and minor quartz and iron oxide phases. There is no alignment of minerals or evidence for strain. Some plagioclase crystals have fractured cores with high-relief polysynthetic twinned cores mantled by lower-relief rims (Fig. 6g). Hornblende occasionally has 0.5- to 1.5-mm relict cores of clinopyroxene with embayed edges. The boundary between altered and unaltered diorite is locally gradational. Therefore, we interpret the altered and unaltered

granitoid east of the shear zone to both represent the Sierra Atacama diorite.

Alteration of the Sierra Atacama diorite involves albitization of plagioclase and replacement of mafic phases by actinolite and epidote. The degree of alteration ranges from pervasive near the shear zone boundary to patchy or incomplete with increasing distance from the shear zone. Textures are locally igneous rather than secondary as evidenced by the preservation of 1- to 2-mm subhedral grains with polysynthetic twinning. Local subhedral to anhedral brown garnet with rims of fluid inclusion-rich actinolite and titanite occur distributed within the pluton and are not connected to obvious veins or fluid pathways (Fig. 6e). These Ca-Fe-bearing phases are mineralogically similar to the assemblage seen in the andradite vein. In other areas, titanite, actinolite, and epidote define compositional bands within zones of secondary feldspar development. Large (> 10 mm), anhedral, internally structureless feldspar with abundant fluid inclusions cross-cut igneous plagioclase with oscillatory zoning and polysynthetic twinning (Fig. 6f). Plagioclase mineral chemistry is discussed below. There is no undulatory extinction, alignment of grain axes, and other evidence of internal strain.

The small-scale intrusions that cut the altered portions of the Sierra Chicharra shear zone and Sierra Atacama diorite are composed of ~ 35–65% hornblende, 30–55% plagioclase, ~ 5–10% quartz, and < 5% potassium feldspar (Fig. 6h). All phases are unaltered with minimal development of epidote and fine-grained white mica within plagioclase and limited replacement of hornblende by biotite.

The undeformed andradite vein cuts annealed mylonitic fabrics. Vein mineralogy is dominantly (90–95%) euhedral brown garnet up to 0.5 cm with lesser subhedral to euhedral green epidote up to 1 cm long, subhedral quartz up to 0.5 cm long, magnetite, and calcite (Fig. 7a). Quartz and epidote are interstitial to garnet, indicating that garnet paragenetically precedes crystallization of quartz and epidote (Fig. 7b). Locally, mineralogy varies to include anhedral masses of 0.5–1 mm apatite cut by anastomosing veins of magnetite. No sulfides are present. There is no evidence of pseudomorphic relationships with previous phases, retrograde alteration, or replacement.

Whole-rock and plagioclase mineral geochemistry

New whole-rock data from this study area and compiled regional geochemical data plot on igneous trends that are distinct between the Coastal Cordillera arc and Copiapó batholith (Fig. 8; ESM Supplementary Data 1). The array of geochemical data from for both magmatic suites defines a range of intermediate to felsic SiO_2 values (between ~ 55 and 75 wt%) with K_2O, FeO*, CaO, and Na_2O trends typical of progressive fractional crystallization. Within the Coastal Cordillera, individual plutons such as the Sierra Chicharra sample a wide range of the SiO_2 compositions that capture the full range of the Coastal Cordillera trend. Our whole-rock geochemical analyses of unaltered Sierra Chicharra pluton and previously published analyses on the unit by Jara et al. (2021a) plot within the field of calc-alkaline magmatism defined by the FeO*/MgO values of Coastal Cordillera arc plutons (Fig. 8) (Marschik et al. 2003). The data for Copiapó batholith extends to more mafic compositions than the Coastal Cordillera and are comparatively tholeiitic in FeO*/MgO values. The Copiapó batholith is particularly different in terms of primary K content, plotting in the high-K fields, whereas the Coastal Cordillera falls within the medium-K range (Fig. 8). The two exceptions to this division of magmatic compositions are the ~ 110 Ma Los Lirios pluton and ~ 108–103 Ma Sierra Pajas Blancas pluton, which geochemically resemble the Coastal Cordillera arc rather than the coeval Copiapó batholith plutons (Fig. 8). The Sierra Atacama diorite falls at the mafic end of the high-K calc-alkaline and ferroan suite that dominates the Copiapó batholith. We note that the composition of the unaltered Sierra Atacama diorite determined in this study (Fig. 8) falls within the field of published data from Girardi (2014) and Jara et al. (2021b) for this pluton at significantly more dispersed sites (locations, Fig. 3, and data, Fig. 8 and ESM Supplementary Data 1). Furthermore, map relationships suggest that sampled outcrops are part of a single continuous pluton. This suggests that zonation of the pluton is not the primary driver of geochemical differences between the altered and unaltered samples seen in this work. The more mafic nature of the younger magmatism is evident in the field: the Coastal Cordillera arc-related Sierra Chicharra pluton is a quartz diorite whereas the unaltered Sierra Atacama is dioritic to gabbroic. Other younger intrusions are relatively more also mafic than the Sierra Chicharra quartz diorite, especially the melanocratic hornblende diorite dike that cuts both the Sierra Chicharra shear zone and the Sierra Atacama diorite.

Two samples from the altered Sierra Chicharra pluton and altered Copiapó batholith samples from across the area, including near Las Pintadas and under the waste pile at Candelaria, reflect the geochemical characteristics of IOCG-related alteration. Element mass gains and losses on alteration cannot be quantitatively determined as no element can be demonstrated to be both immobile and of uniform concentration in each pluton and are thus assessed qualitatively through comparison of compositions of altered rocks relative to the igneous trends (Fig. 8). Relative to unaltered samples, the altered parts of each pluton fall along trends of composition consistent with magnetite-destructive calcic- to sodic-calcic alteration: K_2O is almost quantitatively leached; FeO* is consistently lower; CaO is slightly but consistently higher; and Na_2O is variably and locally strongly higher (Fig. 8 and ESM Supplementary Data 1). The direction and

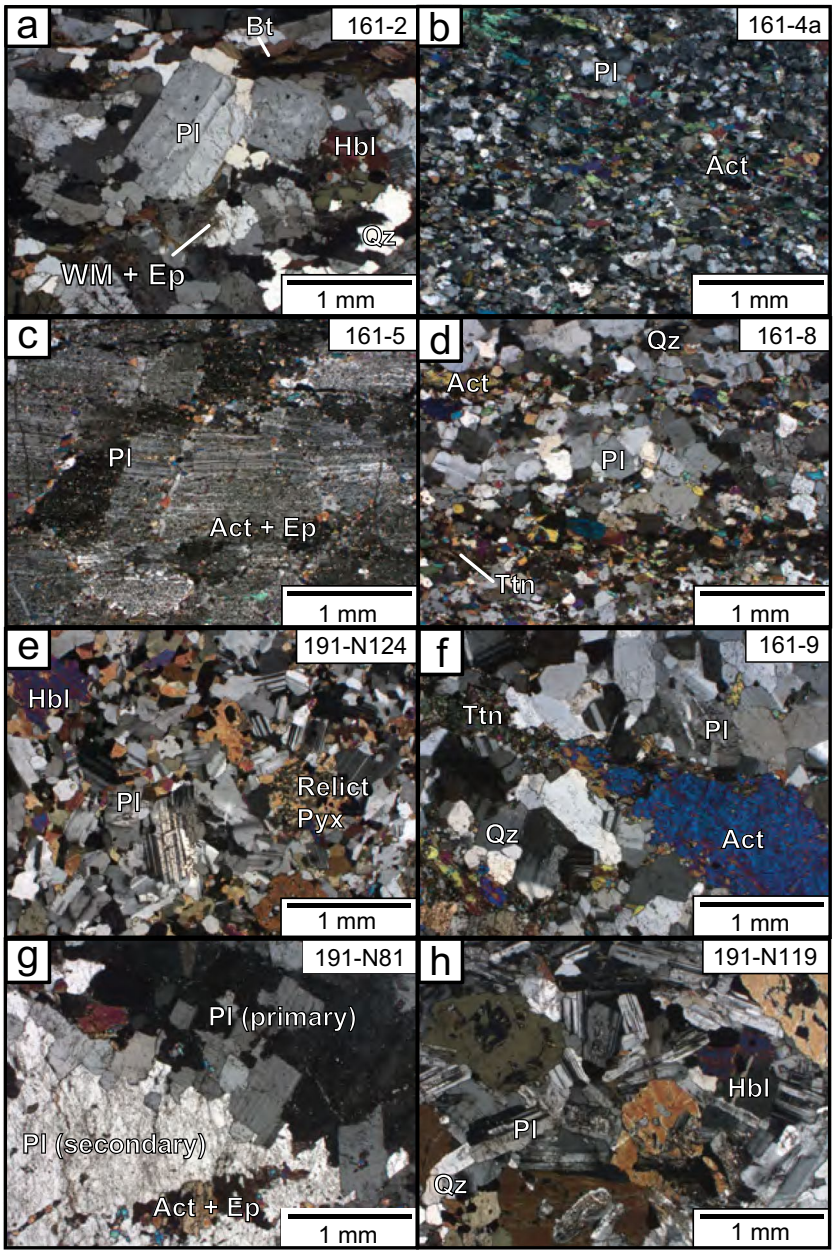

degree of SiO_2 metasomatism cannot be constrained; however, the shifts of CaO and FeO* cannot be simultaneously explained by either SiO_2 addition or loss. Depletion of K_2O and FeO* and synchronous enrichment of Na_2O and CaO can be related to the development of titanite, epidote, and actinolite at the expense of original mafic phases (e.g., biotite and amphibole).

Albitization of whole rocks given by > 1 wt% increase in Na_2O can be seen in the chemistry of the two plagioclase textures (Fig. 6): 1- to 2-mm euhedral to subhedral plagioclase with polysynthetic twinning has An contents of 28 to 37% (average 33.3 ± 1.5%), whereas mm- to cm-scale anhedral, internally structureless plagioclase from three sites across the shear zone has An contents of 23 to 32% (average 26.3 ± 2.2%), 21–25% (average 22.9 ± 0.8%), and 23 to 30% (average 27.8 ± 2.3%) (ESM Supplementary Data 2). While igneous mineral chemistry data is sparse within the studied region, the polysynthetic plagioclase compositions overlap with the low end of plagioclase compositions determined for unaltered Coastal Cordillera arc plutons along the Coloso Fault at the northern end of the Paposo segment near Antofagasta (Fig. 1, An contents of 37–53% for plutons with 54.8 to 59.1 wt% SiO_2) (Lucassen and Franz 1996). The albitization at the whole-rock and mineral scale, in addition to gains and losses in other major elements, is thus similar to deep, peripheral sodic-calcic alteration recorded distal to

◂**Fig. 6** Representative photomicrographs from each map unit. All thin sections are cut perpendicular to foliation, and where a lineation is present, parallel to lineation. **a** Unaltered Sierra Chicharra quartz diorite (sample 161–2). Fine-grained white mica and epidote are present in the cores of some plagioclase. Note the horizontal alignment of biotite defining the weak magmatic foliation seen in Fig. 4a. **b**–**d** Textures within the hydrothermally overprinted mylonitic shear zone organized by increasing distance from the shear zone-Sierra Chicharra contact. Note that all mesoscale mylonitic fabrics are annealed by actinolite + epidote + plagioclase alteration mineralogy. Samples with sub-cm- to mm-scale foliation planes hosted in secondary feldspar are concentrated near the center of the shear zone. **b** Fine-grained lithology (sample 161-4a) with actinolite and secondary plagioclase evenly distributed throughout. **c** Very fine-grained actinolite + epidote overgrown by blocky, internally unstrained secondary plagioclase (sample 161–5). **d** Compositionally distinct bands of actinolite + epidote and plagioclase in the eastern portion of the shear zone (sample 161–8). Strong compositional separation produces the green and white "pinstripe" appearance of mylonites seen in Fig. 4b. **e**–**g** Textures of the unstrained and variably altered Sierra Atacama diorite. **e** Unaltered, unstrained domain of the Sierra Atacama diorite located on the eastern margin of the study area (sample 191-N124). Note the relict cores of clinopyroxene in the hornblende. **f** Titanite + actinolite defines a veinlet within the Sierra Atacama diorite. The texture in the actinolite is formed by abundant fluid and mineral inclusions. **g** Contact zone between two textural types of plagioclase. Primary plagioclase is finer grained and retains polysynthetic twinning whereas secondary feldspar is coarser and lacks internal texture. Mafic phases actinolite + epidote are found within secondary plagioclase. **h** Unaltered, unstrained hornblende diorite dike (sample 191-N119) that cuts the shear zone. Abbreviations are as follows: Act, actinolite; Bt, biotite; Ep, epidote; Hbl, hornblende; Kfs, potassium feldspar; Qz, quartz; Pl, plagioclase; Pyx, pyroxene; Ttn, titanite; WM, white mica. All photomicrographs were taken under cross-polarized light. Whole-rock geochemistry for **a**, **b**, **e**, and **g** is given in Supplementary Data 1 and Fig. 11. Geochemical compositions of plagioclase for **b**, **d**, **e**, and **f** are given in Supplementary Data 2. Zircon U–Pb data for **a**, **e**, and **h** are given in Supplementary Data 3 and Fig. 8

IOCG ore bodies in and around the Copiapó batholith (e.g., Kreiner (2011) and Barton et al. (2011, 2013)).

Zircon U–Pb geochronology

Sierra Chicharra quartz diorite

Individual zircon grains from the unaltered Sierra Chicharra quartz diorite have $^{206}Pb/^{238}U$ dates that fall between ~ 116 and ~ 132 Ma (Fig. 9a; ESM Supplementary Data 3). The concordia age for all concordant zircons is 122.8 ± 0.5 Ma ($n = 33$, MSWD = 3.8). Th/U values consistently cluster around ~ 1 (mean 0.95 ± 0.15; range 0.69–1.29) except for a few grains with a Th/U of ~ 0.23–0.28. Grains with low Th/U are not restricted to a particular date range.

Sierra Atacama diorite

The overall range of zircon U–Pb dates obtained from the Sierra Atacama diorite varies between ~ 104 and 136 Ma. Individual zircon grains analyzed in polished mounts have $^{206}Pb/^{238}U$ dates that range from ~ 119 to 136 Ma (Fig. 9b; ESM Supplementary Data 3). The concordia age determined from grains in polished mounts is 125.9 ± 0.4 Ma ($n = 53$, MSWD = 67). We used cathodoluminescence (CL) imagery to resolve the source of the date dispersion. Zircon textures of the altered domain of the Sierra Atacama diorite are complex. Core domains either retain blurred oscillatory zoning or have convoluted zoning patterns with complex patches of bright and dark CL response. Relatively bright, patchy external or rim domains are characterized by irregular dissolution/recrystallization fronts that cut internal domains and almost completely replace original internal textures in some grains. Complex CL textures on the internal domains of single grains in polished mounts occur in grains across the spread of 118.9 to 136.1 Ma U–Pb dates. All but 2 grains with dates younger than 120 Ma occur in domains with complex internal CL textures. External domains range from 110.3 to 116.2 Ma. Depth profile analysis of additional unpolished zircons to capture internal and rim domains documented dates ranging from ~ 104 to 130 Ma and a concordia age of 117.8 ± 0.4 Ma ($n = 39$, MSWD = 51). Grains have Th/U values ranging from 0.15 to 1.69 (average 1.03 ± 0.42) and do not show systematic variations in Th/U, [U], or degree of discordance with date (ESM Supplementary Data 3).

Cross-cutting hornblende diorite dike in the Sierra Chicharra shear zone

U–Pb dates from individual polished zircon grains in the unaltered, unstrained hornblende diorite dike yielded a range between 114.2 and 132.9 Ma and two slightly older dates (137.2 Ma and 143.1 Ma) from grains with < 10% discordance (Fig. 9c; ESM Supplementary Data 3). The concordia age is 125.0 ± 0.4 Ma ($n = 46$, MSWD = 140). We employed CL imagery and additional depth profiles to better understand the dispersion. Zircon grains from sample 191-N116 are euhedral and have complex internal textures with igneous oscillatory zoning and overgrowths including core and rim relationships, convoluted zoning, and recrystallization fronts similar to those documented in the altered Sierra Atacama diorite. Cores are often bright, with dark inner rims and medium-gray outer rims. Oscillatory zoning is largely replaced by mixed bright and dark domains. Where oscillatory zoning remains, the zones are blurred. Overgrowths are patchy in CL and uniformly medium gray, and in some grains, this patchy, medium-gray texture has replaced the entire zircon structure. Recrystallization fronts are irregular and cross-cut other internal textures. Depth profile analyses yielded a dispersed range of $^{206}Pb/^{238}U$ dates from 100.6 to 132.9 Ma with a concordia age of 120.3 ± 0.4 Ma ($n = 30$, MSWD = 30).

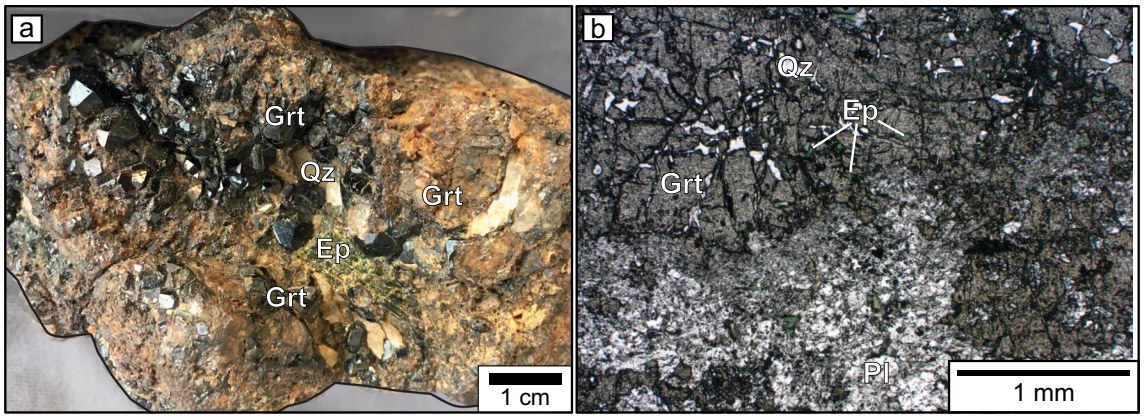

Fig. 7 Petrography and textures from the andradite vein. **a** Photograph showing euhedral crystals of brown garnet with interstitial quartz and epidote. **b** Photomicrograph showing the boundary between the andradite vein and wall rock, composed primarily of plagioclase. Photomicrograph taken under plane-polarized light. Abbreviations are as follows: Ep, epidote; Grt, garnet; Qz, quartz

Garnet U–Pb geochronology and oxygen isotope characterization of the andradite vein

Garnet is dominantly andradite based on EDS analyses (Fig. 10a, ESM Supplementary Data 4). Grandite series compositions such as those found in this vein are favorable for U–Pb analysis due to ferric rather than ferrous Fe content (Gevedon et al. 2018). U concentrations range between 0.23 and 5.3 ppm, and some domains include significant proportions of non-radiogenic or common Pb (Pb_C) in the garnet lattice (ESM Supplementary Data 5). Andradite data were plotted in Tera-Wasserburg space to account for the presence of non-radiogenic Pb. The $^{238}U/^{206}Pb$ lower intercept date is 95.4 ± 2.1 Ma (MSWD = 1.3, n = 38, Fig. 10b), and the $^{207}Pb/^{206}Pb_C$ upper intercept is 0.734 ± 0.030.

Oxygen isotope ratios ($\delta^{18}O$) for quartz, epidote, and garnet mineral separated from within the vein are positive relative to Vienna Standard Mean Ocean Water (+5.7‰ for epidote, + 11.1‰ for quartz, and + 5.4‰ for garnet; ESM Supplementary Data 6). Quartz and epidote are interstitial to garnet (Fig. 7a, b), indicating that the three phases are unlikely to be in equilibrium together. Andradite is primarily stable above 400 °C unless the hydrothermal fluid is high in CO_2, which is unlikely given the presence of epidote in this vein (Taylor and Liou 1978). There is no petrographic evidence for the breakdown of garnet (Fig. 7b). As such, we treat the $\delta^{18}O$ values of garnet separately from the oxygen isotopes of quartz + epidote. Allowing for a maximum hydrothermal temperature bound of 550 °C and a range of temperatures down to 400 °C, the calculated fractionation between grossular-andradite garnet and water is − 3.6 to − 3.9‰ at 400 °C and − 2.9 to − 3.1‰ at 550 °C (Clayton et al. 1972; Matthews 1994; Kohn and Valley 1998). Garnet with $\delta^{18}O$ value of + 5.4‰ is calculated to be formed in equilibrium with fluids with $\delta^{18}O$ values greater than ~ + 8.5‰. Stable isotope thermometry of the quartz-epidote pair ($\Delta_{qtz\text{-}ep}$ = + 5.4‰) suggests crystallization of retrograde minerals at 319 + 14/ − 61 °C (Vho et al. 2020), which represents a minimum fluid temperature for the vein after fluids had begun to cool. The composition of hydrothermal fluid in equilibrium with quartz and epidote over this temperature range is calculated to be approximately + 5.1‰ $\delta^{18}O$. Temperatures calculated from the parameters of Zheng (1993a, b) range from ~ 294 to 298 °C in equilibrium with fluids with $\delta^{18}O$ ratios of + 4.3 to + 4.4‰.

Discussion

Deciphering the age of intrusion from complex zircon U–Pb data

Accurately determining the timing of Sierra Chicharra shear zone activity hinges on the interpretation of the complex U–Pb date distributions recorded in this area. The high MSWD that characterize many of the data sets across the study area, especially in zones affected by hydrothermal alteration, indicate that zircon grains in any sample do not represent single populations, and as such, concordia ages cannot represent the age of intrusion. Here, we carefully examine trends and compare our new data to previous studies to provide robust interpretations of pluton emplacement ages.

Sierra Chicharra quartz diorite

Single-grain zircon $^{206}Pb/^{238}U$ dates have a unimodal population in unaltered Sierra Chicharra sample 161–2 (Fig. 11a).

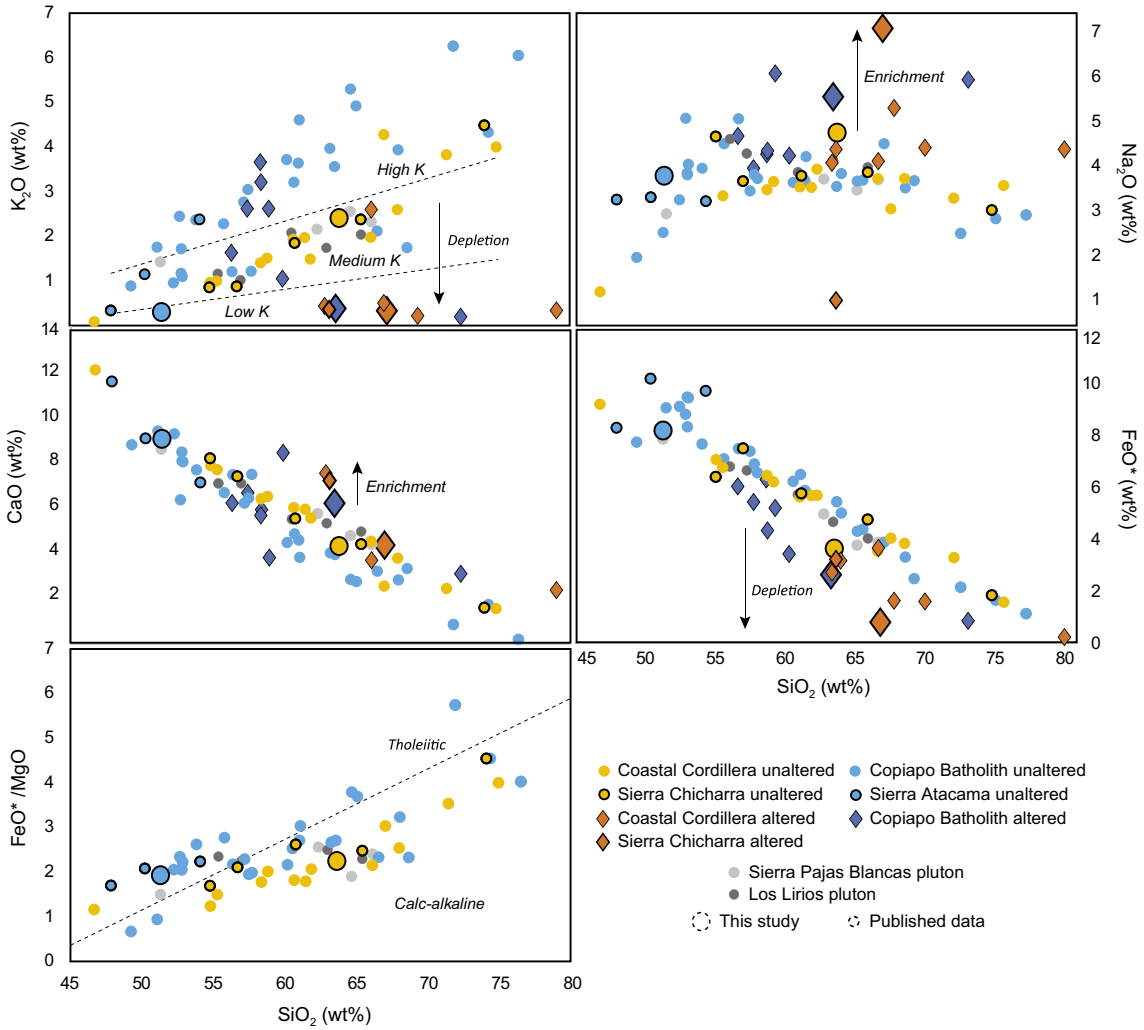

Fig. 8 Bivariate major element vs. SiO_2 diagrams of intrusions in the Copiapó area. FeO* is total Fe as FeO. High-, medium-, and low-K divisions are after Le Maitre et al. (1989); tholeiitic and calc-alkaline fields are after Arculus (2003). Samples from the Coastal Cordillera are given in yellow and orange, and samples from the Copiapó batholith are given in shades of blue. Large symbols are our data, and small symbols show published data from the literature (ESM Supplementary Data 1). Samples with heavy black outlines represent the Sierra Chicharra quartz diorite and Sierra Atacama diorite. The compositions of unaltered Sierra Chicharra correspond with those of all other calc-alkaline intrusions along the Coastal Cordillera arc (yellow circles). The Sierra Atacama diorite falls at the mafic end of the high-K calc-alkaline suite that dominates the Copiapó batholith (light blue circles). Altered rocks from both intrusions (diamonds) fall in a distinct field of low K_2O, somewhat lower FeO*, and higher CaO and Na_2O compared to both igneous trends

The pattern shown by the tails of the distribution matches those expected for small degrees of Pb loss (5 grains in the younger tail, ~ 116–118 Ma) and inheritance (7 grains in the older tail, ~ 126–132 Ma) (Fig. 11a; Spencer et al. 2016). Inheritance is common in long-lived, incrementally assembled arc plutons (e.g., Miller et al. 2007; de Saint Blanquat et al. 2011), and Pb loss is likely related to hydrothermal fluid flow that produced alteration of the nearby shear zone (discussed below). Based on these characteristics, we interpret the weighted mean of the central 21 individual U–Pb dates (122.1 ± 0.6 Ma, $n = 21$; MSWD = 0.68) to be the emplacement age of the Sierra Chicharra quartz diorite in the study area.

This weighted mean date is younger than previously reported biotite K–Ar and $^{40}Ar/^{39}Ar$ dates (i.e., 128–125 Ma) (Arévalo 1995, 2005a; Godoy et al. 2003) and previously reported zircon U–Pb dates (i.e., 126.9 ± 1.1 Ma and 125.3 ± 1.2 Ma) (Jara et al. 2021a) from the Sierra Chicharra quartz diorite. These previous studies sampled the pluton 5–14 km away from our study area, suggesting some degree of spatial variability that may be a product of incremental pluton assembly. Incremental assembly of the Sierra Chicharra is supported by the overlap of individual zircon U–Pb dates reported here with the distributions reported by Jara et al. (2021a) (Fig. 11a), interpreted to represent recycling of antecrysts in the magma chamber.

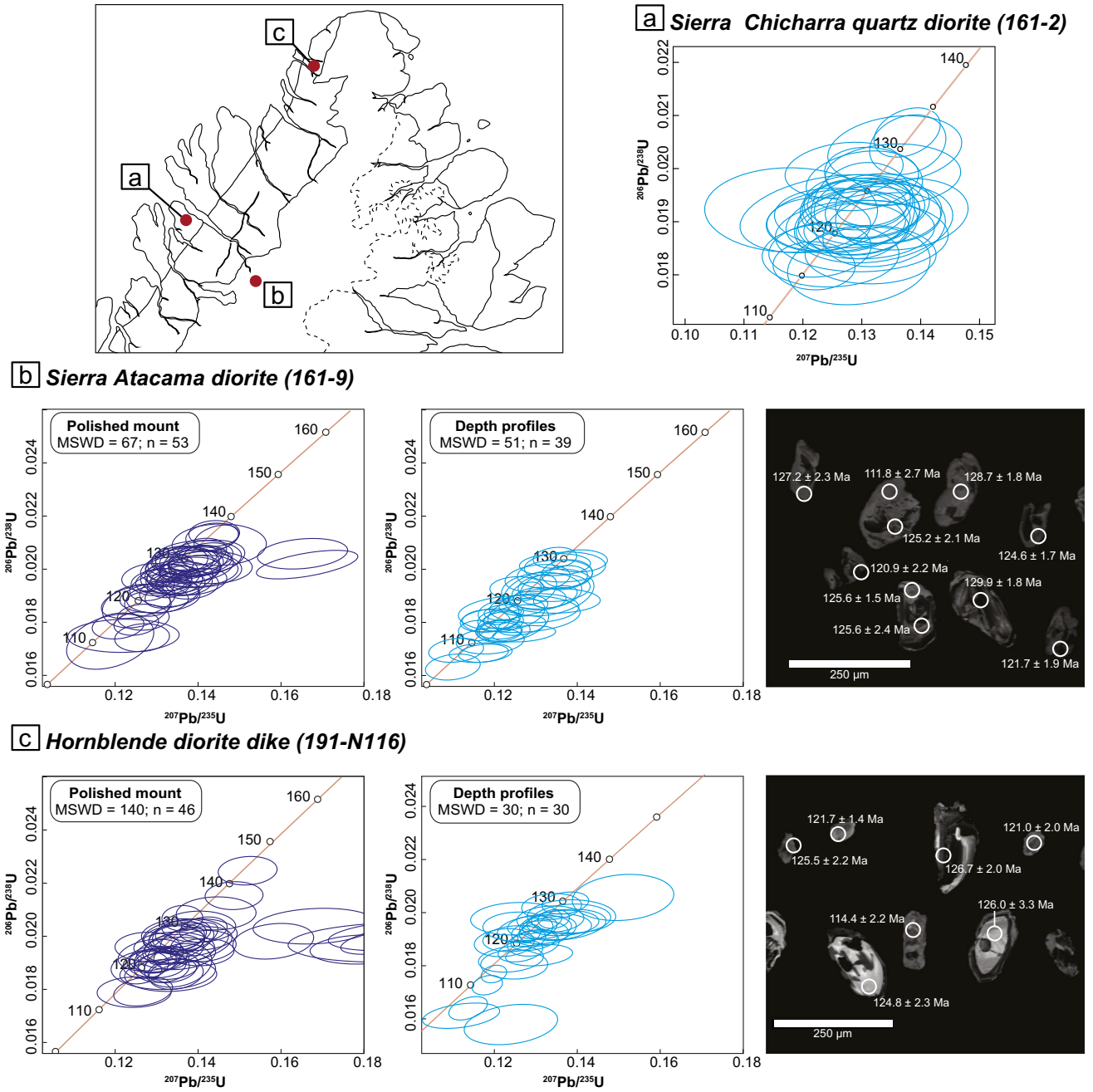

Fig. 9 U–Pb concordia diagrams for zircon from the **a** Sierra Chicharra quartz diorite (sample 161–2), **b** Sierra Atacama diorite (sample 161–9), and **c** hornblende granodiorite dike (sample 191-N116). Ellipses show 2σ uncertainties. Upper left panel reproduces a simplified version of Fig. 3 as an index map for sample locations. Data from polished mounts are plotted separately from depth profiles to show the variation in single-grain analyses from each analysis type. CL images for samples 161–9 and 191-N116 are shown to better understand the source of high MSWD values (for full CL imagery, see Supplementary Fig. 2). Interpretation of zircon U–Pb data is provided in Fig. 11

Construction of the pluton over ~ 3–5 Myr fits with timescales of pluton construction documented elsewhere along the Coastal Cordillera arc (Cruden et al. 2004). Therefore, we interpret the intrusion ages of the overall Sierra Chicharra to range between ~ 126 and 122 Ma, with emplacement of the youngest pulse on the western margin of the Atacama fault system within this study area at 122.1 ± 0.6 Ma (Fig. 11b). Given the presence of a magmatic fabric and concordant transition to mylonitic fabrics across the Sierra Chicharra shear zone, we further interpret this age to represent the minimum bound on inception of ductile deformation along this segment of the AFS.

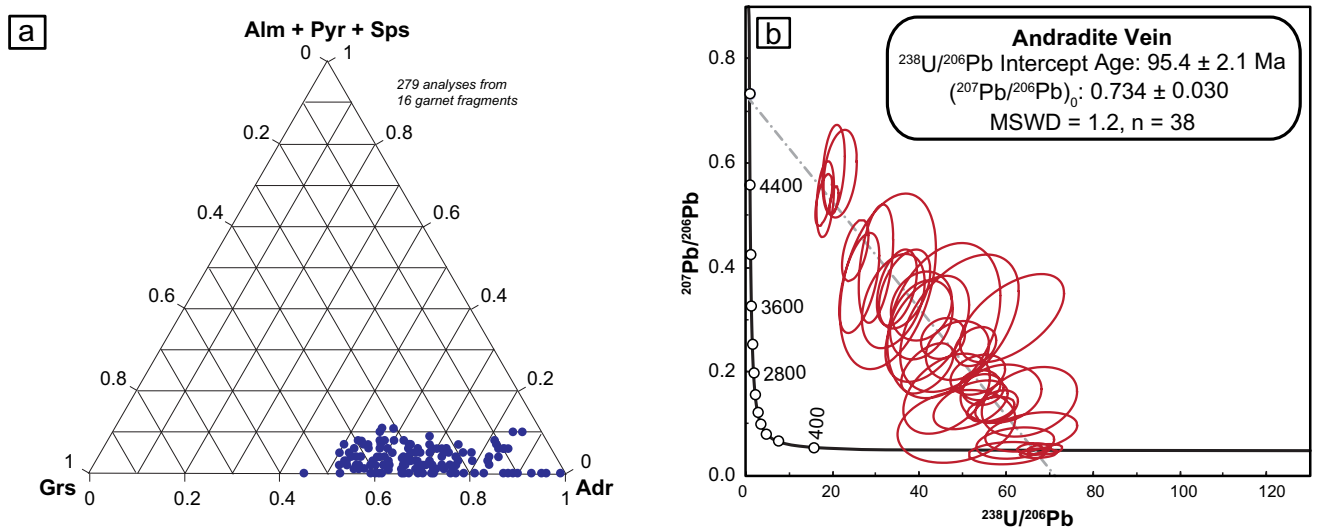

Fig. 10 Composition and U–Pb concordia from the andradite vein. **a** Ternary diagram of garnet compositions determined by energy-dispersive spectroscopy. These qualitative determinations show that the andradite vein is the correct composition for U–Pb geochronology. Geochemical compositions for all 16 garnet fragments analyzed for U–Pb are given in Supplementary Data 4. **b** Tera-Wasserburg diagram for andradite U–Pb data. $^{238}U/^{206}Pb$ lower-intercept age and $^{207}Pb/.^{206}Pb_0$ composition are reported. Full garnet U–Pb data given in Supplementary Data 5

Sierra Atacama diorite

Zircon $^{206}Pb/^{238}U$ data from the altered domain of the Sierra Atacama diorite (sample 161–9) show an older peak from 136 to 120 Ma with an overlapping younger shoulder from 120 to 105 Ma when plotted as a kernel density estimate (Fig. 11a). Reducing the bandwidth on the kernel density estimate allows the distribution to be resolved into two peaks. Narrowing the discordance filter from < 10 to < 2% to focus on only the most concordant data reduces the height of the older peak relative to the younger shoulder but does not resolve the complexity of the distribution. A multi-modal distribution indicates that the zircons are not derived from a single pulse of magma and may contain a significant component of inherited zircons. The main peak in the age spectra (~ 136–120 Ma) overlaps the distribution of zircons from the Sierra Chicharra quartz diorite (Fig. 11a). Inheritance of mineral grains from a prior magma is also shown by the preservation of clinopyroxene and plagioclase cores in the unaltered Sierra Atacama diorite (Fig. 6e).

The younger cluster with a ~ 120–110 Ma range of dates overlaps with (a) the age of interpreted minor Pb loss in the Sierra Chicharra quartz diorite and (b) recent zircon U–Pb dates from exposures of unaltered Sierra Atacama diorite from ~ 5.5 km southeast of the Sierra Chicharra shear zone (114.6 ± 0.3 Ma and 113.9 ± 0.5 Ma) (Jara et al. 2021a), ~ 7.5 km southeast of the Sierra Chicharra shear zone (114.8 ± 0.5 Ma, 114.5 ± 0.5 Ma, and 111.6 ± 0.6 Ma) (Jara et al. 2021a) and a K–Ar date of 117–104 Ma (Arévalo 2005a, b). Internal textures of the Sierra Atacama diorite in Jara et al. (2021a) show simple and/or oscillatory zoning (Fig. 2 of Jara et al. (2021a)). These grains are euhedral with angular crystal faces and do not show the irregular, gray domains cross-cutting igneous textures seen in our study (e.g., Fig. 9b and ESM Fig. 2). The textures of the zircon presented by Jara et al. (2021a) support an igneous origin without a substantial fluid overprint. Additionally, their single-grain data range between ~ 113 and 117 Ma and do not show an older or younger population (Fig. 11a) (Fig. 4F of Jara et al. 2021a). Therefore, we propose that the comparison to their data set is robust approach to interpret the complex data in this work. Integrating field relationships with published geochronology, we interpret a 114.0 ± 0.6 Ma zircon U–Pb emplacement date based on a coherent population of 14 concordant zircons ($n = 14$, MSWD = 1.6, Fig. 11c). Given the lack of solid-state fabrics in the Sierra Atacama diorite and pervasive alteration of the western margin of the pluton, we further interpret this age to represent the minimum bound on the end of Sierra Chicharra shear zone activity and maximum bound on the phase of hydrothermal fluid flow that caused alteration of this pluton.

We interpret individual zircon U–Pb dates younger than ~ 110 Ma to record disturbance of the U–Pb system post-dating emplacement of the pluton. This interpretation is based on several factors: ample field and petrographic evidence for syn-emplacement hydrothermal alteration, as well as complex CL patterns in many grains younger than ~ 110 Ma. Non-uniform CL response with complex bright and dark cores reflects internal heterogeneities in rare earth element concentrations including

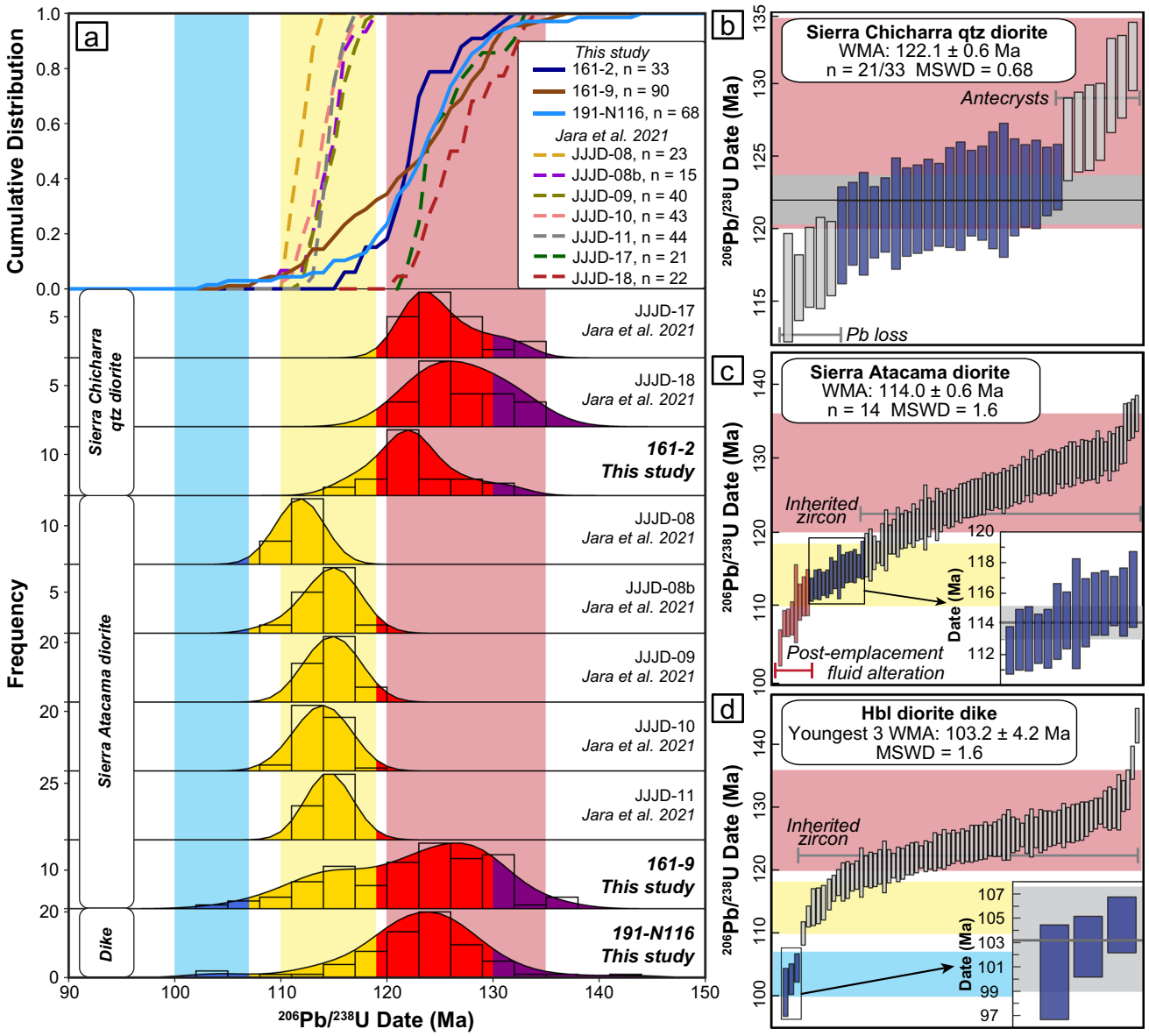

Fig. 11 **a** Cumulative distribution functions (CDF) and kernel density estimates for zircon U–Pb data from the Sierra Chicharra quartz diorite, Sierra Atacama diorite, and hornblende granodiorite dike. Samples from this study are compared to data from Jara et al. (2021a). Red and yellow bars mark the inflection points in the CDF. Plots made using DetritalPy (Sharman et al. 2018). Weighted mean dates for zircon from the **b** Sierra Chicharra quartz diorite (sample 161–2), **c** Sierra Atacama diorite (sample 161–9), and **d** hornblende granodiorite dike (sample 191-N116). Bars denoting the extent of single-grain dates for the Sierra Chicharra and Sierra Atacama plutons from the CDF are shown on the weighted mean plots. Grains used to determine the weighted mean date are shown in blue, grains affected by hydrothermal alteration are shown in red, and inherited or antecrystic grains are shown in gray. Where data are complex, weighted mean determinations are shown in the inset plots. See text for discussion

U distribution (e.g., Rubatto and Gebauer 2000) as well as variability in the diffusion domain size and lattice-controlled diffusion pathways within individual crystals. Post-emplacement alteration younger than ~ 110 Ma is further supported by the lack of zircon $^{206}Pb/^{238}U$ dates between 110 and 105 Ma in the unaltered hornblende diorite dike that cuts the zone of alteration (discussed below).

Cross-cutting hornblende diorite dike in the Sierra Chicharra shear zone

Single-grain $^{206}Pb/^{238}U$ dates from dike sample 191-N116 show a multi-modal distribution with the largest peak between 135 and 120 Ma, a small but distinct peak from 120 to 110 Ma, and a minor peak from 105 to 100 Ma. This pattern overlaps with the distribution of individual

zircon U–Pb dates from the Sierra Chicharra quartz diorite and single-grain dates from the unaltered Sierra Atacama diorite of Jara et al. (2021a) (Fig. 11a). We note the absence of single-grain dates between ~ 110 and 105 Ma, which further supports an intrusion age of the Sierra Atacama diorite by ~ 114 Ma with hydrothermal alteration producing the ~ 110–104 Ma range of dates.

Despite the preponderance of zircon U–Pb dates 115 Ma and older, cross-cutting field relationships clearly document the intrusion of this dike post-dated the cessation of mylonitization and alteration of the Sierra Chicharra shear zone (Fig. 4c). As such, we interpret most zircon grains from this dike to be inherited xenocrysts from the surrounding plutons (Fig. 11d). Significant inheritance of zircon can be expected in < 10-m-wide intrusive bodies whose contact zones cool too rapidly to dissolve inherited zircon (Bindeman and Melnik 2016). The youngest three analyses do not overlap with the distributions seen in either the Sierra Chicharra or Sierra Atacama plutons, and therefore, we interpret them to record the intrusion of the dike. The three youngest analyses give a weighted average of 103.2 ± 4.2 Ma (MSWD = 1.6, Fig. 11d). Although the precision of this age is low, it does support the cross-cutting field relationships and overlaps the age of the nearby Sierra Pajas Blancas intrusion of Jara et al. 2021a (99.6 ± 1.5 Ma, 99.2 ± 0.7 Ma). As such, we interpret the last phase of hydrothermal alteration to end prior to intrusion of this dike at ~ 103 Ma.

Andradite vein

All analytical spots for andradite fall along a single linear array in Tera-Wasserburg space (Fig. 10b). Given that selected spots spanned multiple garnet crystals and targeted transects across individual crystals, this variation along a single line suggests all garnet crystals formed in one event over a relatively short time span. The spread along the array reflects differing proportions of radiogenic (U-derived) Pb versus non-radiogenic (common) Pb. Therefore, the lower intercept of 95.4 ± 2.1 Ma is interpreted to record the timing of andradite vein crystallization (Fig. 10b).

Geometry, kinematics, and timing of the Sierra Chicharra shear zone

Integrating field relationships and geochronologic data outlines the following series of deformation and pluton emplacement events (Fig. 12) associated with the AFS in the Copiapó region: (1) synkinematic emplacement of the Coastal Cordillera arc-related Sierra Chicharra quartz diorite at 122.1 ± 0.6 Ma and development of the mylonitic Sierra Chicharra shear zone during AFS-related strain, (2) post-kinematic emplacement of the Copiapó batholith-related Sierra Atacama diorite at 114.0 ± 0.6 Ma, and (3) post-kinematic intrusion of several hornblende granodiorite stocks and dikes, one of which intruded at 103.2 ± 4.2 Ma. Cross-cutting relationships combined with the interpretation of zircon U–Pb ages constrain shear zone activity between ~ 122 and 114 Ma, overlapping IOCG mineralization in the Punta del Cobre district and transpressional motion on syn-mineralization structures throughout the district (del Real et al. 2023).

Synkinematic emplacement of the Sierra Chicharra quartz diorite during AFS strain is evidenced by magmatic fabrics within the pluton west of the shear zone transitioning to concordant protomylonitic fabrics across the western margin of the shear zone and ultimately to ultramylonites within the core of the Sierra Chicharra shear zone (Figs. 4 and 5d). Coaxial fabrics and S-tectonites record flattening normal to the shear zone with sparse sinistral kinematic indicators and apparent sinistral and reverse kinematics along late-stage shear bands. Where lineations are present, they primarily plunge NE along the NW-dipping shear zone. The orientation of mylonitic fabric with regard to the trend of the shear zone boundary shows a symmetric distribution with a bias towards a clockwise orientation, suggesting a minor component of sinistral shear, consistent with outcrop-scale indicators (Fig. 13a). Overall, these geometric and kinematic data indicate that mylonitic fabrics developed in a coaxial-dominated transpressional strain regime with sinistral shear (Fig. 13b) (e.g., Sanderson and Marchini 1984; Fossen and Calvalcante 2017). Coaxial-dominated transpressional zones are typically characterized by vertical lineations (e.g., Tikoff and Greene 1997; Fossen and Calvalcante 2017); however, shallowly plunging lineations may suggest some strain partitioning with the sinistral component focused in some domains and the coaxial component dominant elsewhere. Sinistral transpression ended prior to the intrusion of the unstrained Sierra Atacama diorite. Locally, veinlets within the hydrothermally altered Sierra Atacama diorite define a spaced fabric subparallel to the shear zone boundary, which may suggest that the pluton intruded at the end stages of deformation or may alternatively reflect emplacement-related flow.

Multiple pulses of hydrothermal fluid flow

Field observations and microstructural relationships document three pulses of hydrothermal fluid flow resulting in the growth of alteration assemblages: (1) synkinematic Na-Ca alteration associated with AFS sinistral shear during and after emplacement of the Sierra Chicharra quartz diorite between 122 and 114 Ma, (2) post-kinematic Na-Ca alteration coeval with intrusion of the Sierra Atacama diorite at ~ 114 Ma, and (3) a sub-km-scale hydrothermal andradite vein through the center of the annealed Sierra Chicharra

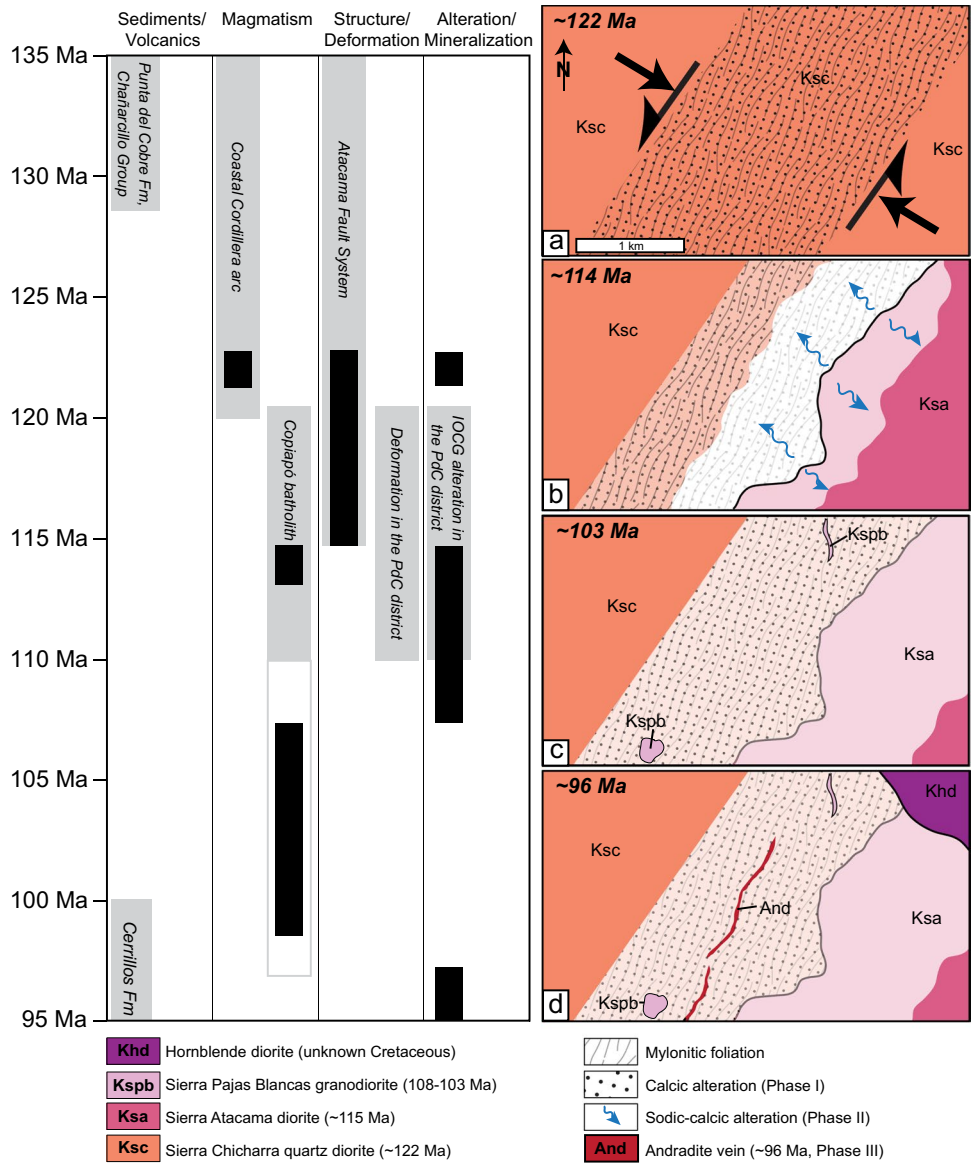

Fig. 12 Left: temporal evolution of sedimentation, magmatism, deformation, and alteration in the Copiapó region. Gray bars give timing constraints from previous work; black bars indicate new timing constraints from this study. Note the correlation between Copiapó batholith magmatism, deformation in the wider Punta del Cobre district, and development of IOCG alteration. Atacama fault system deformation is correlated with Coastal Cordillera arc magmatism and ends during the period of IOCG-related alteration. Right: schematic map of events along the Sierra Chicharra shear zone. **a** Intrusion of the ~ 122 Ma Sierra Chicharra quartz diorite is associated with the development of ~ 200–500-m-wide NW-dipping sinistral shear zone as documented by a progression from magmatic fabrics within the pluton to protomylonitic to ultramylonitic fabrics along the main branch of the AFS. A first phase of alteration is associated with shearing, recorded by internally strained actinolite and elongate titanite aligned parallel to foliation planes. **b** Cessation of deformation by ~ 114 Ma, documented by the intrusion of the unstrained Sierra Atacama diorite that cuts all mylonitic fabrics. Annealing of mylonitic fabrics in the shear zone and sodic-calcic alteration of the western margin of the unstrained diorite record a post-kinematic second phase of alteration associated with the intrusion of the Sierra Atacama diorite. **c** Two phases of intrusions cut annealed shear zone fabrics between ~ 103 and 95 Ma: several small hornblende granodiorite bodies within the shear zone and a larger unstrained hornblende diorite that cross-cuts the shear zone, altered Sierra Atacama diorite, and unaltered Sierra Atacama diorite. **d** A third phase of alteration is marked by the development of an ~ 775-m-long post-kinematic andradite vein through the center of the annealed shear zone at ~ 95 Ma

shear zone at ~ 95 Ma, post-dating all intrusions at the current level of exposure (Fig. 12). The timing of alteration is compatible with known alteration and mineralization events documented throughout the Punta del Cobre district, including an early stage associated with emplacement of an Early Cretaceous Coastal Cordillera pluton, a major stage related to emplacement of La Brea diorite at ~ 117 Ma, and a final stage at ~ 115 Ma hosted in the San Gregorio

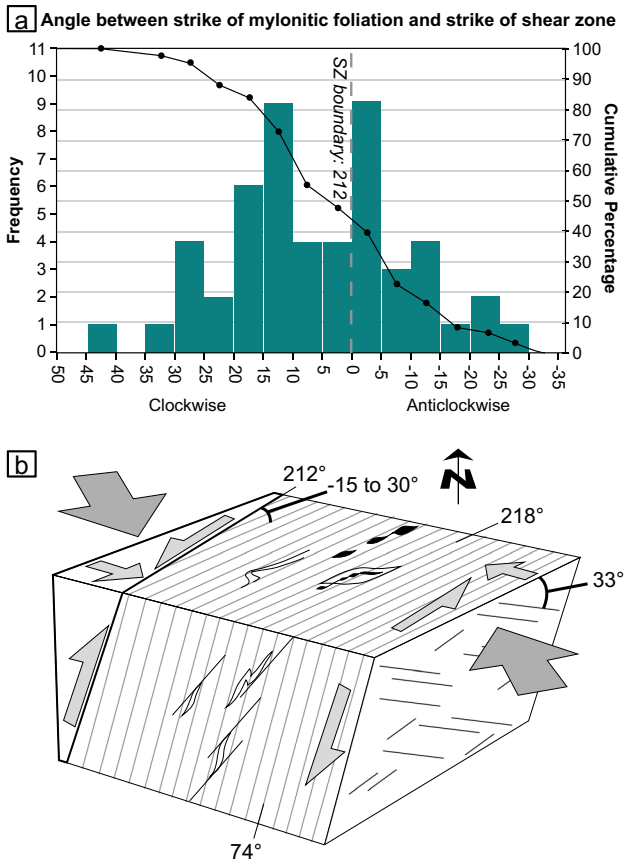

Fig. 13 **a** Histogram showing the angle between the shear zone boundary and mylonitic foliation. **b** Block diagram showing the spatial distribution of kinematic indicators in the shear zone. Shear sense indicators on the top surface are shown in Fig. 5a, shear sense indicators on the vertical surface are shown in Fig. 5b, and the orientation of the foliation and lineations are taken from Fig. 5d. Arrows show shear needed to produce these kinematic indicators, documenting an overall transpressional setting

monzodiorite (Zentilli 1974; Marschik et al. 1997; Ullrich and Clark 1999; Marschik et al. 2003; Marschik and Sollner 2006; Kreiner 2011; Girardi 2014).

Petrographic textures in the annealed shear zone indicate two phases of alteration assemblage development: synkinematic and post-kinematic. The first pulse of alteration is recorded by elongate actinolite, epidote, and titanite aligned with the relict mylonitic fabric in the Sierra Chicharra shear zone. It is possible that these phases are pseudomorphs after elongated phases present in the original mylonitized mineral assemblage; however, we interpret alteration to be synkinematic based on textures indicating deformation and annealing of alteration minerals, including undulatory extinction in actinolite, which records intracrystalline strain during ongoing deformation. Large, blocky plagioclase with relatively albitic compositions (average 23–28% An) pinned between or enveloping compositional bands that define the annealed mylonitic fabrics represents a second phase of alteration within the study area. The lack of undulatory extinction or internal strain within albitic plagioclase, presence of Na-Ca minerals within the altered domain of the Sierra Atacama diorite, disturbance of zircon U–Pb dates, and shifts in whole-rock geochemistry including the increase in Na_2O and CaO and loss of FeO* and K_2O indicate extensive sodic-calcic alteration along the western margin of the Sierra Atacama diorite associated with the intrusion of Copiapó batholith-related magmas. Similar alteration of a mylonite zone associated with the AFS is documented at Cerro Negro Norte and Cerro Iman, ~ 40 km and ~ 22 km north of the studied area (Raab 2001). Many plutons from this magmatic phase were constructed by multiple phases of intrusion resulting in significant internal zonation (e.g., Rodríguez et al. 2019), and the possibility remains that the altered western margin and unaltered exposure of the Sierra Atacama diorite may have had significantly different unaltered compositions.

Formation of the unaltered, undeformed andradite vein documents a third pulse of hydrothermal fluid flow at ~ 95 Ma (Fig. 12). It is further possible that some of the alteration within the Sierra Atacama diorite is coeval with this third phase of fluid flow. The vein shares many characteristics with Punta del Cobre IOCG deposits, including carbonate-associated veins hosted in dioritic plutons in the Jesús María, Ojancos Viejo, and Ojancos Nuevo districts (Kreiner 2011) and mineralized andradite-bearing assemblages at Alcaparrosa, Atacama Kozan, and Candelaria (e.g., del Real et al. 2018). Prograde garnet dominates at IOCG deposits such as San Antonio (Fréraut and Cuadra 1994) and is paragenetically equivalent to potassium feldspar + albite + quartz and biotite + magnetite assemblages in contiguous andesitic volcanic rocks at Panulcillo at the southern end of the Chilean Iron Belt (Hopper and Correa 2000). The andradite vein developed ~ 20 Myr after the economically important ~ 115 Ma mineralization event in the Punta del Cobre district based on cross-cutting relationships and geochronology of intrusive phases, but possibly at the same time as the latest minor magmatism in the area. Copiapó batholith magmatism continued until ~ 97 Ma, and potential sources for the magmatic-hydrothermal fluids include the ~ 98 Ma hypabyssal hornblende clinopyroxene diorite (Arévalo 2005a, b) or ~ 110–99 Ma Sierra Pajas Blancas intrusions (Jara et al. 2021a) mapped ~ 5 km to the north.

Composition and temperature of hydrothermal fluids recorded by the andradite vein

In contrast with the pervasive alteration throughout the shear zone, the andradite vein has sharp contacts with the wall rock which indicates focused fluid flow along an

opening-mode conduit that may have been a result of high fluid pressures as hydrothermal fluids exsolved from an underlying pluton. This suggests that the isotopic signatures of the andradite vein have the lowest degrees of contamination with wall rock and can yield insights into the fluids responsible for hydrothermal alteration. The garnet value of + 5.4‰ and calculated range of hydrothermal fluid compositions ($\delta^{18}O > +8.5$‰) indicate formation in a system dominated by fluids in equilibrium with a magmatic source (ESM Supplementary Data 6). These trends support recent work by Tornos et al. (2020) suggesting hydrothermal fluids sourced from residual melts enriched in Ca, Mg, Si, and Ti, and volatiles are responsible for the development of regional alkali-calcic alteration assemblages.

Petrographic textures indicate that garnet was the first mineral to crystallize, followed by epidote, quartz, and calcite. We note that the measured oxygen isotope ratios of quartz (+ 11.1‰) are close to the range documented for main-stage mineralization at Candelaria (+ 11.2 to + 12.6‰ quartz oxygen isotope ratios; Marschik et al. 2000). Fluid inclusions from Candelaria homogenize at 370–440 °C (Marschik et al. 2000). Stable isotope thermometry of the quartz-epidote pair in the andradite vein cutting the Sierra Chicharra shear zone suggests crystallization in equilibrium with + 4.3 to + 5.1‰ $\delta^{18}O$ fluids at ~ 290–320 °C, below the fluid inclusion homogenization temperature at Candelaria. The calculated composition of the hydrothermal fluid from which quartz precipitated is more depleted in ^{18}O by comparison with garnet values, indicating quartz formed at lower temperatures. Depletion in ^{18}O could reflect a progressive influx of cooler meteoric fluid with time as the magmatically driven hydrothermal system collapsed.

Magmatically driven IOCG-related alteration during regional transpressional deformation

Marschik and Fontboté (2001a), Chen et al. (2013), and Richards et al. (2017) proposed that IOCG and IOA deposits of northern Chile and southern Peru formed during a period of relatively mafic (gabbrodioritic to dioritic) arc magmatism related to a phase of transtensional tectonism. Our observations, set in the context of previous work, support the spatial and temporal link between regional sodic-calcic alteration in the Punta del Cobre district and the transition to relatively mafic, K-rich ferroan Copiapó batholith magmatism following typical calc-alkaline Coastal Cordillera arc magmatism. Globally, links between IOCG mineralization and K-rich mafic magmatism are also proposed at the Norrbotten district of Sweden (Martinsson et al. 2016), Alemão deposit of Brazil (Perelló et al. 2023), Great Bear magmatic zone of Canada (Ootes et al. 2017), and Gawler Craton of Australia (e.g., Budd and Skirrow (2007)).

Repeated pulses of sodic-calcic alteration associated with the intrusion of Copiapó batholith plutons have been documented across the Punta del Cobre district, with each intrusion producing its own hydrothermal system (e.g., Kreiner 2011). Regionally, sodic-calcic alteration developed at shallow crustal levels (≤ 4–6 km) and occurs both along the margins of plutons and along major structures (e.g., Kreiner 2011; Barton et al. 2013). The volumetrically most important stage of hydrothermal alteration along the Sierra Chicharra shear zone was due to fluids exsolved from or fluid circulation associated with the ~ 114 Ma Sierra Atacama diorite of the Copiapó batholith. Sodic-calcic alteration along the Sierra Chicharra shear zone matches district-scale alteration with pervasive, texturally destructive replacement of igneous host rocks by fine- to medium-grained albite, actinolite or diopside, magnetite, and hydrothermal titanite with local rutile cores (e.g., Camus 1980; Ryan et al. 1995; Marschik and Fontboté 2001a; Barton et al. 2005, 2011; Kreiner 2011). The temperatures and stable isotope compositions of the hydrothermal fluids in the Sierra Chicharra shear zone match those forming the IOCG mineralization. The andradite vein displays textures supporting a low degree of fluid/rock interaction and formation in an open conduit as a result of high fluid pressures. Focused alteration of the shear zone and adjoining marginal parts of the cross-cutting Sierra Atacama diorite indicates fluids exploited the strong subvertical anisotropy of foliation planes along the transcrustal AFS (e.g., Tornos et al. 2020) in addition to pluton margins as fluid pathways to facilitate the rapid ascent to shallow depths.

Ductile deformation in the Copiapó region is localized at the margins of Early Cretaceous plutons, as is seen along the El Salado segment to the north (e.g., Seymour et al. 2020). A notable difference between the Sierra Chicharra shear zone in this study compared to elsewhere along the El Salado segment is the distinct lack of brittle faults overprinting mylonitic fabrics. We attribute the lack of brittle faulting to protracted magmatism in this area compared to the rest of the El Salado segment. The Copiapó batholith represents the largest area of magmatic rocks along the AFS that intruded after ~ 120 Ma (Fig. 2) (Arévalo 2005a; Jara et al. 2021a, this work). The continued intrusion of magmatic bodies maintained elevated geothermal gradients in this area beyond the end of slip along the El Salado segment (e.g., Seymour et al. 2020). Annealing of mylonitic fabrics and coarse grain sizes of secondary plagioclase formed during alteration indicates high temperature, magmatically derived fluid flow both outlived and post-dated deformation. Although Sierra Chicharra shear zone activity between ~ 122 and 114 Ma is coeval with alteration and mineralization in the Punta del Cobre district, the hydrothermal fluids in the shear zone experienced a much higher degree of wallrock interaction by percolating pervasively along the ~ 200–300-m-wide shear zone. The

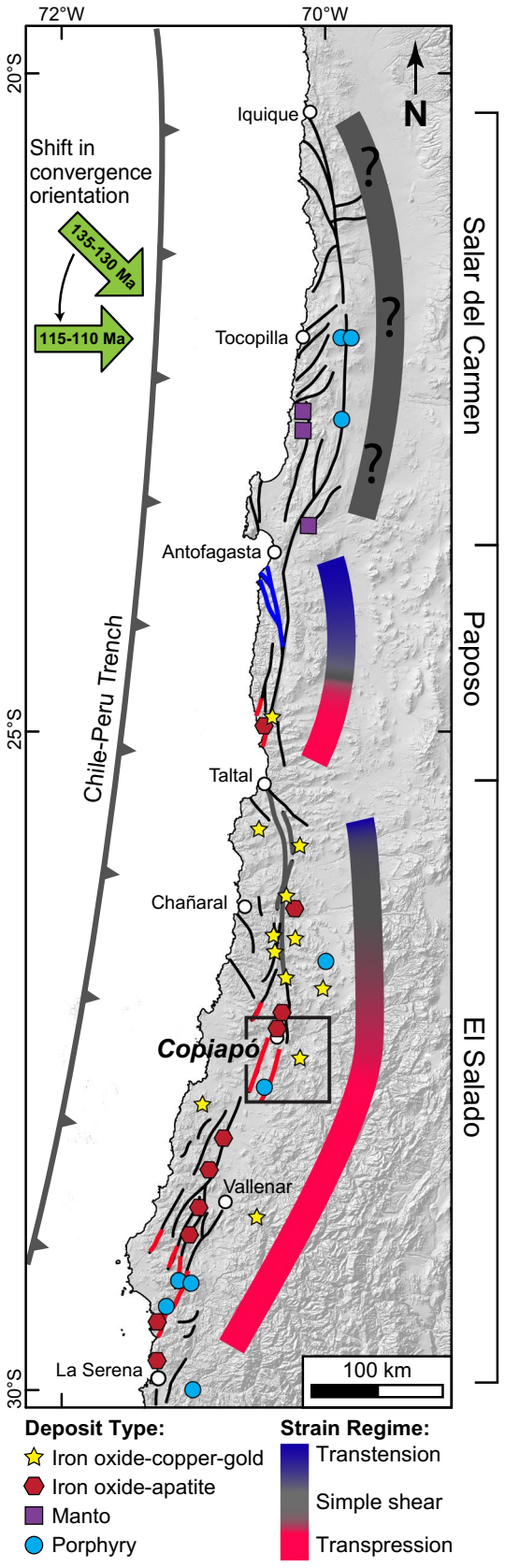

Fig. 14 Modern-day topography, trace of AFS-related faults, and locations of economic deposits from Fig. 1. Strain regime bows are added along the AFS to present a regional picture of the interaction between fault strike, convergence vector at ~ 135–130 Ma from Scheuber and Andriessen (1990), convergence vector at ~ 115–110 Ma from Maloney et al. (2013), and strain regime. The geometry of the bows matches the geometry of the AFS fault branches through each part of the fault system. Fault segments are color-coded to show the distribution of transtensional (blue), lateral only (gray), or transpressional (red) strain. Strain regime is derived from the following studies: Northern Paposo segment, Veloso et al. (2015); Paposo fault, Ruthven et al. (2019); northern and central El Salado segments, Seymour et al. (2021); Copiapó section of the El Salado segment, this work; Punta del Cobre district, del Real et al. (2018); and southern El Salado segment, Heuser et al. (2020)

more dispersed flow along the transcrustal fluid pathways may have prevented the formation of an economic deposit.

The overall patterns of AFS-related sinistral displacement are consistent with a uniform Early Cretaceous SE-directed oblique convergence vector that imparted a NW–SE component of shortening across the N-striking Peru–Chile trench accommodated within the Coastal Cordillera (Fig. 14). Within this overall setting, the varying orientations of fault branches relative to the convergence vector produce either transtension, lateral motion without significant extension or compression, or transpression. NNW- to NW-striking structures at the northern end of the Paposo segment (Cembrano et al. 2005; Veloso et al. 2015; Masoch et al. 2021) accommodate sinistral transtension. Along much of the northern and the central El Salado segment north of Copiapó where the dominant trend of the AFS is ~ N-S, sinistral shear dominates and with no evidence for widespread transpression nor transtension (Seymour et al. 2021). Where the major faults shift to in orientation to NNE and NE strikes along the southern end of the Paposo segment, mylonitic fabrics record shear zone-perpendicular flattening and oblique sinistral-reverse shear in a transpressional strain field (Ruthven et al. 2019). The patterns and timing of strain in the Sierra Chicharra shear zone are consistent with sinistral transpression overlapping with the formation of IOCG deposits in the adjacent Punta del Cobre district.

The distribution of deposit types along the AFS also shows a broad correlation with the orientation of the major structures: IOCG deposits are concentrated along the N-S striking segment of the El Salado segment whereas IOA and porphyry deposits are concentrated along the NE-striking segment (Fig. 14). While some northern Chilean IOCG deposits along the AFS are hosted along locally extensional structures such as extensional duplexes (Cerro Negro Norte, Dominga, Elgueta et al. 1990; Raab 2001; Veloso et al. 2017) or transtensional stepovers (Mantoverde, Vila et al. 1996; Rieger et al. 2010), our observations in the Copiapó area do not support the development of these hydrothermal systems in an overall transtensional tectonic regime.

This study instead documents transpression across the AFS between ~ 122 and 114 Ma, which overlaps with the late stages of deformation along the AFS (Ruthven et al. 2019; Seymour et al. 2020). The orientation of the AFS shifts from N-S striking to NE striking at the latitude of Copiapó and corresponds with a regional shift from purely sinistral strike-slip motion to sinistral transpression. Transpression across the AFS also corroborates recent work showing main-stage mineralization at ~ 122–115 Ma during transpression along in the Candelaria-Punta del Cobre district (de Real et al. 2018, 2023), development of IOCG-related veins during transpressional reactivation of the El Tofo fault system at ~ 121 Ma (Creixell et al. 2011, 2020), and precipitation of copper ores under a transpressional regime at the Dominga Fe-Cu deposit at the southern end of the El Salado segment (Heuser et al. 2020).

The development of IOCG-related mineralization during crustal shortening is also documented in the Norrbotten IOA-IOCG province of northern Sweden, where early extensional structures accommodated the development of IOA deposits and IOCG mineralization followed during a temporally distinct phase of basin inversion and shortening (Andersson et al. 2021). Similarly, IOCG mineralization at Alemão in the Igarapé Bahia camp of Brazil is interpreted to have occurred during or immediately following basin inversion of the Carajas basin in the Amazon craton (Perelló et al. 2023). Across the Andean IOCG clan, Chen et al. (2013) document a major IOCG mineralization synchronous with basin inversion. These findings collectively suggest that while local extensional to transtensional structures may be important during the early stages of IOA-IOCG deposit formation from magmatically derived hydrothermal fluids (e.g., Barra et al. 2017), a regional extensional or transtensional regime is not required for IOCG mineralization and shortening or transpression may dominate at a district scale.

Conclusions

Our results document the timing of magmatism, Atacama fault system deformation, and sodic-calcic alteration and related IOCG mineralization in the Punta del Cobre district near Copiapó, Chile. Intrusion of the ~ 122 Ma Sierra Chicharra quartz diorite of the Coastal Cordillera arc is associated with the development of the ~ 200–300-m-wide NW-dipping sinistral Sierra Chicharra shear zone that defines the AFS, as documented by a progression from magmatic fabrics within the pluton to protomylonitic and ultramylonitic fabrics. The geometry and kinematics indicate ductile shear occurred in a sinistral transpressional regime. Deformation ceased by ~ 114 Ma, documented by the intrusion of the unstrained Sierra Atacama diorite of the Copiapó batholith that cuts all mylonitic fabrics. Two phases of intrusions cut annealed shear zone fabrics: several small hornblende granodiorite bodies within the shear zone and a larger unstrained hornblende diorite that intrudes both the shear zone and the unstrained Sierra Atacama diorite. These and other plutons comprise the Early Cretaceous (119–97 Ma) Copiapó batholith, a pulse of more mafic, high-K ferroan magmatism that outlasted more typical calc-alkaline Coastal Cordillera magmatism documented elsewhere along the northern El Salado segment of the AFS. Continuation of magmatism into the latest Albian near Copiapó kept temperatures at exposed levels above the brittle-plastic transition during AFS shear and prevented the development of a major brittle fault.

The Sierra Chicharra shear zone served as a potentially transcrustal pathway for hydrothermal fluids which gave rise to sodic-calcic alteration over several intervals in the Cretaceous. An initial phase (126–122 Ma to > 114 Ma) of alteration is associated with the synkinematic intrusion and mylonitization of the eastern margin of the Sierra Chicharra quartz diorite during the final phases of AFS-related transpressional deformation as the plate motion vector shifted from southeast directed to east–west directed. The Sierra Chicharra shear zone is cut by the unstrained Sierra Atacama diorite. Synkinematic hydrothermal alteration is recorded by internally strained actinolite and elongate titanite aligned parallel to foliation planes. A second phase of hydrothermal alteration overprinted the Sierra Chicharra shear zone beginning at ~114 Ma. This post-kinematic event is associated with the intrusion of the Sierra Atacama diorite during the early stages of Copiapó batholith magmatism and corresponds to a transition to more orthogonal shortening across the convergent margin. This phase is volumetrically the most important and is recorded by annealing of mylonitic fabrics defined by sodic-calcic alteration assemblages in the shear zone and by secondary plagioclase and sodic-calcic alteration near the western margin of the unstrained diorite. This alteration occurred before intrusion of the unaltered hornblende granodiorite intrusions during the latest phases of Copiapó batholith magmatism at ~ 103 Ma. Finally, the development of an ~ 775-m-long post-kinematic andradite vein through the center of the annealed shear zone marks a pulse of magmatic-hydrothermal fluid at ~ 95 Ma possibly also associated with the last phases of magmatism in the batholith. All phases of alteration were formed from fluids that are likely equivalent to those responsible for IOCG mineralization of the Punta del Cobre district and related sodic-calcic alteration assemblages in the deep, peripheral zones of the district. Notably, mineralization-related hydrothermal fluid flow utilized the prominent steeply dipping mylonitic fabrics of the shear zone in lieu of a brittle fault, leading to pervasive and dispersed hydrothermal activity such that it did not result in the development of an economic deposit along the AFS studied.

In the context of previous studies of the tectonic regime of both the AFS as a whole and northern Chilean deposits in particular, this work contributes to the growing recognition that an extensional or transtensional tectonic regime is not required for the formation of IOCG deposits. Instead, the IOCG-related alteration hosted along the Sierra Chicharra shear zone, Punta del Cobre district, and other districts between 27.4° S and 30° S occurs along an overall NE-striking segment of the Atacama fault system. Over the time period when the Sierra Chicharra shear zone was actively deforming with sinistral transpressional strain (~ 122–114 Ma), IOCG mineralization was occurring in the adjacent Punta del Cobre district (~ 122–115 Ma), and the northern Chilean margin was entering the latest stages of SE-directed oblique convergence before transitioning to more E-W directed orthogonal convergence.

Supplementary Information The online version contains supplementary material available at https://doi.org/10.1007/s00126-024-01259-2.

Acknowledgements The authors would like to thank M. Hernandez for field assistance, D. Adams for SEM assistance at USGS Denver, D. Burns for EMPA assistance at Stanford, and L. Stockli for laboratory assistance at UT-Austin. G. Heuser, Y. Kuiper, J. Hourigan, M. Grove, A. Pamucku, and J. Barnes are thanked for helpful discussions. The authors would like to thank N. Jansson, F. Tornos, N. Oliver, J. Andersson, and two anonymous reviewers for their detailed and constructive feedback on this manuscript.

Author contribution N. Seymour, J. Singleton, R. Gomila, and G. Arancibia contributed to the study conception and design. Field-based data collection and analysis was performed by N. Seymour, J. Singleton, R. Gomila, and G. Arancibia. Laboratory-based material preparation and data collection were performed by N. Seymour and M. Gevedon. Data analysis was performed by N. Seymour, J. Ridley, J. Singleton, M. Gevedon, S. Seman, and D. Stockli. The first draft of the manuscript was written by N. Seymour, and all authors commented on previous versions of the manuscript. All authors read and approved the final manuscript.

Funding Open access funding provided by SCELC, Statewide California Electronic Library Consortium This work was funded by National Science Foundation Grant #1822064 to J. Singleton and Society of Economic Geologists Student Research Grant to N. Seymour. G. Arancibia acknowledges funding from Millennium Nucleus Center for Metal Tracing Along Subduction NC #130065. Part of this work was performed at the Stanford Nano Shared Facilities (SNSF), supported by the National Science Foundation under award ECCS-2026822.

Data Availability Sample materials from this work are archived at Colorado State University and can be obtained by contacting J. Singleton.

Code availability Not applicable.

Declarations

Competing interests The authors declare no competing interests.

References

Aguirre-Urreta MB, Mourgues FA, Rawson PF, Bulot LG, Jaillard E (2007) The Lower Cretaceous Chañarcillo and Neuquén Andean basins: ammonoid biostratigraphy and correlations. Geol J 42:143–173

Allmendinger RW, Cardozo N, Fisher DM (2011) Structural geology algorithms: vectors and tensors. Cambridge University Press

Amilibia A (2009) Compressional deformation along the Chañarcillo basin west margin: North Chilean Late Jurassic-Early Cretaceous back-arc basin. Trabajos de Geología 29:78–83

Andersson JB, Bauer TE, Martinsson O (2021) Structural evolution of the central Kiruna area, Northern Norrbotten, Sweden: implications on the geologic setting generating iron oxide-apatite and epigenetic iron and copper sulfides. Econ Geol 116(8):981–2009

Arculus RJ (2003) Use and abuse of the terms calcalkaline and calcalkalic. J Petrol 44:929–935

Arévalo C (1994) Mapa geológico de la Hoja Los Loros, Región de Atacama. Servicio Nacional de Geología y Minería, Carta Geológica de Chile

Arévalo C (1995) Mapa geológico de la Hoja Copiapó, Región de Atacama. Servicio Nacional de Geología y Minería, Carta Geológica de Chile

Arévalo C (1999) The Coastal Cordillera/Precordillera boundary in the Tierra Amarilla area (27° 20′ 27 40′S/70° 05′–70 20′W), northern Chile, and the structural setting of the Candelaria Cu-Au ore deposit. Dissertation, University of Queens

Arévalo C (2005a) Carta Copiapó, Región de Atacama. Servicio Nacional de Geología y Minería, Carta Geológica de Chile

Arévalo C (2005b) Carta Los Loros, Región de Atacama. Servicio Nacional de Geología y Minería. Carta Geológica de Chile

Arévalo C, Creixell C (2009) The Atacama fault system and its role on the formation of IOCG and magnetite-apatite ores: an evaluation from the Los Choros and Huasco valleys, northern Chile. XII Congreso Geológico Chileno

Arévalo C, Grocott J, Martin W, Pringle M, Taylor G (2006) Structural setting of the Candelaria Fe-oxide Cu-Au deposit, Chilean Andes (27°30' S). Econ Geol 101:819–841

Barra F, Reich M, Selby D, Rojas P, Simon A, Salazar E, Palma G (2017) Unraveling the origin of the Andean IOCG clan: a Re-Os isotope approach. Ore Geol Rev 81:62–78

Barton MD (2014) Iron oxide (–Cu–Au–REE–P–Ag–U–Co) systems. Treatise on Geochemistry (2nd ed) 13:515–541

Barton MD, Johnson DA (2000) Alternative brine sources for Fe-oxide(-Cu-Au) systems: Implications for hydrothermal alteration and metals. In: Porter TM (ed) Hydrothermal Iron Oxide Copper-Gold & Related Deposits: A Global Perspective. Australian Mineral Foundation, Adelaide, pp 43–60

Barton MD, Jensen EP, Ducea M (2005) Fluid sources for IOCG (Candelaria, Punta del Cobre) and porphyry Cu-Style mineralization, Copiapó batholith, Chile: geologic and Sr isotopic constraints. Geological Society of America Annual Meeting, Salt Lake City, UT

Barton MD, Kreiner DC, Jensen EP, Girardi JD (2011) Multiple igneous-related hydrothermal systems and related IOCG mineralization, near Copiapó, Chile. XI SGA Biennial Meeting 521–523

Barton MD, Johnson DA, Kreiner DC, Jensen EP (2013) Vertical zoning and continuity in Fe oxide (-Cu-Au-Ag-Co-UP-REE) (or 'IOCG') systems: Cordilleran insights. Proceedings of the 12th Biennial Meeting, Society for Geology Applied to Ore Deposits 1348–1351

Barton M, Johnson D (1996) Evaporitic-source model for igneous-related Fe oxide–(REE-Cu-Au-U) mineralization. Geology 24:259–262

Berg K, Baumann A (1985) Plutonic and metasedimentary rocks from the coastal range of northern Chile: Rb-Sr and U-Pb isotopic systematics. Earth Planet Sci Lett 75:101–115

Bindeman IN, Melnik OE (2016) Zircon survival, rebirth and recycling during crustal melting, magma crystallization, and mixing based on numerical modelling. J Petrol 57:437–460

Brown M, Diaz F, Grocott J (1993) Displacement history of the Atacama fault system 25°00′ S–27°00′ S, northern Chile. Geol Soc Am Bull 105:1165–1174

Budd AR, Skirrow RG (2007) The nature and origin of gold deposits of the Tarcoola goldfield and implications for the central Gawler gold province, South Australia. Econ Geol 102(8):1541–1563

Butterworth N, Steinberg D, Müller RD, Williams S, Merdith AS, Hardy S (2016) Tectonic environments of South American porphyry copper magmatism through time revealed by spatiotemporal data mining. Tectonics 35:2847–2862

Camus F (1980) Posible modelo genético para los yacimientos de cobre del distrito minero Punta del Cobre. Andean Geol 11:51–76

Cardozo N, Allmendinger RW (2013) Spherical projections with OSX-Stereonet. Comput Geosci 51:193–205

Cembrano J, González G, Arancibia G, Ahumada I, Olivares V, Herrera V (2005) Fault zone development and strain partitioning in an extensional strike-slip duplex: a case study from the Mesozoic Atacama fault system, northern Chile. Tectonophysics 400:105–125

Cembrano J, Garrido A, Marquardt M (2009) Tectonic setting of IOCG deposits in the Central Andes: strike-slip-dominated deformation. XII Congreso Geologico Chileno

Chen HY, Cooke DR, Baker MJ (2013) Mesozoic iron oxide copper-gold mineralization in the Central Andes and the Gondwana supercontinent breakup. Econ Geol 108:37–44

Chiaradia M, Banks D, Cliff R, Marschik R, De Haller A (2006) Origin of fluids in iron oxide–copper–gold deposits: constraints from $\delta^{37}Cl$, $^{87}Sr/^{86}Sr_i$ and Cl/Br. Miner Deposita 41:565–573

Clayton RN, O'Neil JR, Mayeda TK (1972) Oxygen isotope exchange between quartz and water. J Geophys Res 77:3057–3067

Coira B, Davidson J, Mpodozis C, Ramos V (1982) Tectonic and magmatic evolution of the Andes of northern Argentina and Chile. Earth Sci Rev 18:303–332

Creixell C, Parada M, Morata D, Vásquez P, Pérez de Arce C, Arriagada C (2011) Middle-Late Jurassic to Early Cretaceous transtension and transpression during arc building in Central Chile: evidence from mafic dike swarms. Andean Geol 38:37–63

Creixell C, Fuentes J, Bierma H, Salazar E (2020) Tectonic setting of Cretaceous porphyry copper deposits of northern Chile (28°-30° S) and its relations with magmatic evolution and metallogeny. Andean Geol 47:469–507

Cruden A, Carlos A, Davis D, Grocott J (2004) Timescales and mechanisms of batholith construction, Coastal Cordillera, northern Chile, from precise U–Pb zircon ages and regional geochronological data. AGU Fall Meeting Abstracts

Dallmeyer RD, Brown M, Grocott J, Taylor GK, Treloar PJ (1996) Mesozoic magmatic and tectonic events within the Andean plate boundary zone, 26°–27° 30′ S, North Chile: constraints from $^{40}Ar/^{39}Ar$ mineral ages. J Geol 104:19–40

Daroch GA, Barton MD (2011) Hydrothermal alteration and mineralization in Santo Domingo Sur iron oxide (-Cu-Au) (IOCG) deposit, Atacama Region. 11th SGA Biennial Meeting, Chile, 488–490

de Saint BM, Horsman E, Habert G, Morgan S, Vanderhaeghe O, Law R, Tikoff B (2011) Multiscale magmatic cyclicity, duration of pluton construction, and the paradoxical relationship between tectonism and plutonism in continental arcs. Tectonophysics 500:20–33

del Real I, Thompson JF, Carriedo J (2018) Lithological and structural controls on the genesis of the Candelaria-Punta del Cobre Iron Oxide Copper Gold district, northern Chile. Ore Geol Rev 102:106–153

del Real I, Allmendinger RW, Thompson JF, Creixell C (2023) Evidence for transpression during formation of the Candelaria Punta del Cobre IOCG-district and regional implications. J South Am Earth Sci 126:104289

Elgueta S, Hodgkin A, Rodriguez E, Schneider A (1990) The Cerro Negro mine, Chile: manto-type copper mineralization in a volcaniclastic environment. In: Fontboté L (ed) Stratabound ore deposits in the Andes. Springer, Berlin Heidelberg, pp 463–471

Espinoza S (1990) The Atacama-Coquimbo ferriferous belt, northern Chile. In: Fontboté L (ed) Stratabound ore deposits in the Andes. Springer, Berlin, pp 353–364

Farrar E, Clark AH, Haynes SJ, Quirt GS, Conn H, Zentilli M (1970) K-Ar evidence for the post-Palaeozoic migration of granitic intrusion foci in the Andes of northern Chile. Earth Planet Sci Lett 9:17–28

Fossen H, Cavalcante GCG (2017) Shear zones–a review. Earth Sci Rev 171:434–455

Fréraut R, Cuadra W (1994) Mineralización de Fe, Cu y Au en la franja cretácica de la Costa. Regiones III y IV de Chile. Actas 7th Congr Geol Chileno 2:1046–1050

Gelcich S, Davis DW, Spooner ETC (2005) Testing the apatite-magnetite geochronometer: U-Pb and $^{40}Ar/^{39}Ar$ geochronology of plutonic rocks, massive magnetite-apatite tabular bodies, and IOCG mineralization in northern Chile. Geochim Cosmochim Acta 69:3367–3384

Gevedon M, Seman S, Barnes JD, Lackey JS, Stockli DF (2018) Unraveling histories of hydrothermal systems via U-Pb laser ablation dating of skarn garnet. Earth Planet Sci Lett 498:237–246

Girardi JD (2014) Comparison of Mesozoic magmatic evolution and iron oxide (-copper-gold)('IOCG') mineralization, Central Andes and western North America. Dissertation, University of Arizona

Godoy E, Marquardt C, Blanco N (2003) Carta Caldera, Región de Atacama. Serie Geología Básica, No. 76. Servicio Nacional de Geología y Minería. Santiago

Grocott J, Taylor GK (2002) Magmatic arc fault systems, deformation partitioning and emplacement of granitic complexes in the Coastal Cordillera, north Chilean Andes (25 30' S to 27 00' S). J Geol Soc London 159:425–443

Grocott J, Brown M, Dallmeyer RD, Taylor GK, Treloar PJ (1994) Mechanisms of continental growth in extensional arcs: an example from the Andean plate-boundary zone. Geology 22:391–394

Haynes DW (2000) Iron oxide copper (-gold) deposits: their position in the deposit spectrum and modes of origin. In: Hydrothermal Iron Oxide Copper-gold and Related Deposits: A Global Perspective, vol 1. Australian Mineral Foundation, pp 71–90

Heuser G, Arancibia G, Veloso E, Cembrano J, Cordeiro P, Nehler M, Bracke R (2020) The evolution of the Dominga Fe-Cu deposit

(northern Chile): insights from mineral textures and micro-CT analysis. Ore Geol Rev 119:103316
Hopper D, Correa A (2000) The Panulcillo and Teresa de Colmo copper deposits: two contrasting examples of Fe-ox Cu-Au mineralization from the Coastal Cordillera of Chile. In: Porter TM (ed) Hydrothermal Iron Oxide Copper-gold and Related Deposits: A Global Perspective, vol 1. Australian Mineral Foundation, pp 177–189
Jackson SE, Pearson NJ, Griffin WL, Belousova EA (2004) The application of laser ablation-inductively coupled plasma-mass spectrometry to in situ U-Pb zircon geochronology. Chem Geol 211:47–69
Jaffey AH, Flynn KF, Glendenin LE, Bentley WC, Essling AM (1971) Precision measurement of half-lives and specific activities of ^{235}U and ^{238}U. Phys Rev C 4:1889–1906
Jaillard E, Soler P, Carlier G, Mourier T (1990) Geodynamic evolution of the northern and central Andes during early to middle Mesozoic times: a Tethyan model. J Geol Soc 147:1009–1022
Jara JJ, Barra F, Reich M, Morata D, Leisen M, Romero R (2021a) Geochronology and petrogenesis of intrusive rocks in the Coastal Cordillera of northern Chile: insights from zircon U-Pb dating and trace element geochemistry. Gondwana Res 93:48–72
Jara JJ, Barra F, Reich M, Leisen M, Romero R, Morata D (2021b) Episodic construction of the early Andean Cordillera unravelled by zircon petrochronology. Nature Comm 12:1–8
Kohn MJ, Valley JW (1998) Effects of cation substitutions in garnet and pyroxene on equilibrium oxygen isotope fractionations. J Metam Geol 16:625–639
Kreiner DC (2011) Epithermal style iron oxide (-copper-gold)(= IOCG) vein systems and related alteration. Dissertation, University of Arizona
Lopez GP, Hitzman MW, Nelson EP (2014) Alteration patterns and structural controls of the El Espino IOCG mining district, Chile. Miner Deposita 49:235–259
Lucassen F, Franz G (1996) Magmatic arc metamorphism: petrology and temperature history of metabasic rocks in the Coastal Cordillera of northern Chile. J Metam Geol 14:249–265
Le Maitre RW, Bateman P, Dudek A, Keller J, Lameyre J, Le Bas MJ, Sabine PA, Schmid R, Sorensen H, Streckeisen A, Woolley AR (1989) A classification of igneous rocks and glossary of terms. Recommendations of the IUGS Subcommission on the Systematics of Igneous rocks. Cambridge University Press
Maksaev V, Munizaga F, Valencia V, Barra F (2009) LA-ICP-MS zircon U-Pb geochronology to constrain the age of post-Neocomian continental deposits of the Cerrillos Formation, Atacama Region, northern Chile. Andean Geol 36:264–287
Maloney KT, Clarke GL, Klepeis KA, Quevedo L (2013) The Late Jurassic to present evolution of the Andean margin: drivers and the geological record. Tectonics 32:1049–1065
Marquardt M, Cembrano J, Siña A, Garrido (2009) IOCG-type deposits in North-Central Chile: a case study and implications for exploration. XII Congreso Geologico Chileno
Marschik R, Fontboté L (2001a) The Candelaria-Punta del Cobre iron oxide Cu-Au(-Zn-Ag) deposits, Chile. Econ Geol 96:1799–1826
Marschik R, Fontboté L (2001b) The Punta del Cobre formation, Punta del Cobre-Candelaria area, northern Chile. J South Am Earth Sci 14:401–433
Marschik R, Kendrick MA (2015) Noble gas and halogen constraints on fluid sources in iron oxide-copper-gold mineralization: Mantoverde and La Candelaria, northern Chile. Miner Deposita 50:357–371
Marschik R, Söllner F (2006) Early cretaceous U-Pb zircon ages for the Copiapó plutonic complex and implications for the IOCG mineralization at Candelaria, Atacama Region, Chile. Miner Deposita 41:785–801
Marschik R, Singer BS, Munizaga F, Tassinari C, Moritz R, Fontboté L (1997) Age of Cu(-Fe-Au) mineralization and thermal evolution of the Punta del Cobre district, Chile. Miner Deposita 32:531–546
Marschik R, Fontignie D, Chiaradia M, Voldet P (2003) Geochemical and Sr–Nd–Pb–O isotope composition of granitoids of the Early Cretaceous Copiapó plutonic complex (27° 30′ S), Chile. J South Am Earth Sci 16:381–398
Marschik R, Leveille RA, Martin, W (2000) La Candelaria and the Punta del Cobre district, Chile: Early Cretaceous iron oxide Cu-Au(-Zn-Ag) mineralization. In: Porter TM (ed) Hydrothermal iron-oxide copper-gold & related deposits: A global perspective: Adelaide, Australian Mineral Foundation, 163–175
Martínez F, Arriagada C, Peña M, del Real I, Deckart K (2013) The structure of the Chañarcillo Basin: an example of tectonic inversion in the Atacama region, northern Chile. J South Am Earth Sci 42:1–16
Martinsson O, Billström K, Broman C, Weihed P, Wanhainen C (2016) Metallogeny of the Northern Norrbotten Ore Province, northern Fennoscandian Shield with emphasis on IOCG and apatite-iron ore deposits. Ore Geol Rev 78:447–492
Masoch S, Gomila R, Fondriest M, Jensen E, Mitchell T, Pennacchioni G, Cembrano J, Di Toro G (2021) Structural evolution of a crustal-scale seismogenic fault in a magmatic arc: the Bolfin fault zone (Atacama fault system). Tectonics 40, e2021TC006818
Mathur R, Marschik R, Ruiz J, Munizaga F, Leveille R (2002) Age of mineralization of the Candelaria Fe-oxide Cu-Au deposit and the origin of the Chilean iron belt, based on Re-Os isotopes. Econ Geol 97:59–71
Matthews A (1994) Oxygen isotope geothermometers for metamorphic rocks. J Metamorph Geol 12:211–219
Matthews KJ, Seton M, Müller RD (2012) A global-scale plate reorganization event at 105–100 Ma. Earth Planet Sci Lett 355:283–298
Mavor SP, Singleton JS, Gomila R, Heuser G, Seymour NM, Williams SA. Arancibia G, Johnston SM, Kylander-Clark ARC, Stockli DF (2020) Timing, kinematics, and displacement of the Taltal fault system, northern Chile: implications for the Cretaceous tectonic evolution of the Andean margin. Tectonics 39, e2019TC005832
Miller JS, Matzel JEP, Miller CF, Burgess SD, Miller RB (2007) Zircon growth and recycling during the assembly of large, composite arc plutons. J Volcan Geotherm Res 167:282–299
Mourgues FA (2004) Advances in ammonite biostratigraphy of the marine Atacama basin (Lower Cretaceous), northern Chile, and its relationship with the Neuquén basin, Argentina. J South Am Earth Sci 17:3–10
Mpodozis C, Allmendinger RW (1993) Extensional tectonics, Cretaceous Andes, northern Chile (27°S). Geol Soc Am Bull 105:1462–1477
Mpodozis C, Kay SM (1992) Late Paleozoic to Triassic evolution of the Gondwana margin: evidence from Chilean Frontal Cordilleran batholiths (28°S to 31°S). GSA Bull 104:999–1014
Mpodozis C, Ramos V (1990) The Andes of Chile and Argentina. In: Ericksen GE, Cañas Pinochet MT, Reinemund JA (eds) Geology of the Andes and its relation to hydrocarbon and mineral resources, vol 11. Circum-Pacific Council for Energy and Mineral Resources Earth Science Series, Houston, TX
Naranjo JA, Hervé F, Prieto X, Munizaga F (1984) Actividad cretácica de la Falla de Atacama al este de Chañaral: Milonitización y plutonismo. Comunicaciones 34:57–66
Oliveros V, Morata D, Aguirre L, Feraud G, Fornari M (2010) Jurassic to Early Cretaceous subduction-related magmatism in the Coastal Cordillera of northern Chile (18°30'-24°S): geochemistry and petrogenesis. Revista Geológica De Chile 34:209–232
Ootes L, Snyder D, Davis WJ, Acosta-Góngora P, Corriveau L, Mumin AH, Gleeson SA, Samson IM, Montreuil JF, Potter E, Jackson VA (2017) A Paleoproterozoic Andean-type iron oxide copper-gold environment, the Great Bear magmatic zone, Northwest Canada. Ore Geol Rev 81:123–139

Palma G, Barra F, Reich M, Simon AC, Romero R (2020) A review of magnetite geochemistry of Chilean iron oxide-apatite (IOA) deposits and its implications for ore-forming processes. Ore Geol Rev 126:103748

Parada MA, López-Escobar L, Oliveros V, Fuentes F, Morata D, Calderón M, Aguirre L, Féraud G, Espinoza F, Moreno H, Figueroa O, Muñoz Bravo J, Tronscoso Vásquez R, Stern CR (2007) Andean magmatism. In: Gibbons W (ed) Moreno T. The Geology of Chile, The Geological Society, London, pp 115–146

Paton C, Hellstrom J, Paul B, Woodhead J, Hergt J (2011) Iolite: freeware for the visualisation and processing of mass spectrometric data. J Analyt Atom Spectr 26:2508–2518

Perelló J, Zulliger G, García A, Creaser RA (2023) Revisiting the IOCG geology and age of Alemão in the Igarapé Bahia camp, Carajás province, Brazil. J South Am Earth Sci 124:104273

Petrus JA, Kamber BS (2012) VizualAge: a novel approach to laser ablation ICP-MS U-Pb geochronology data reduction. Geostand Geoanalyt Res 36:247–270

Raab AK (2001) Geology of the Cerro Negro Norte Fe-oxide (Cu-Au) district, Coastal Cordillera, northern Chile. Thesis, Oregon State University

Ramos VA, Folguera A (2009) Andean flat-slab subduction through time. Geol Soc, London, Spec Publ 327:31–54

Richards JP, López GP, Zhu JJ, Creaser RA, Locock AJ, Mumin AH (2017) Contrasting tectonic settings and sulfur contents of magmas associated with Cretaceous porphyry Cu±Mo±Au and intrusion-related iron oxide Cu-Au deposits in northern Chile. Econ Geol 112:295–318

Rieger AA, Marschik R, Díaz M, Hölzl S, Chiaradia M, Akker B, Spangenberg JE (2010) The hypogene iron oxide copper-gold mineralization in the Mantoverde district, northern Chile. Econ Geol 105:1271–1299

Rieger AA, Marschik R, Diaz M (2012) The evolution of the hydrothermal IOCG system in the Mantoverde district, northern Chile: new evidence from microthermometry and stable isotope geochemistry. Miner Deposita 47:359–369

Rodríguez N, Díaz-Alvarado J, Fernández C, Fuentes P, Breitkreuz C, Tassinari CCG (2019) The significance of U-Pb zircon ages in zoned plutons: the case of the Flamenco pluton, Coastal Range batholith, northern Chile. Geosci Front 10:1073–1099

Rodriguez-Mustafa MA, Simon AC, del Real I, Thompson JF, Bilenker LD, Barra F, Bindeman I, Cadwell D (2020) A continuum from iron oxide copper-gold to iron oxide-apatite deposits: Evidence from Fe and O stable isotopes and trace element chemistry of magnetite. Econ Geol 115:1443–1459

Rubatto D, Gebauer D (2000) Use of cathodoluminescence for U-Pb zircon dating by ion microprobe: some examples from the Western Alps. In: Pagel M, Barbin V, Blanc P, Ohnenstetter D (eds) Cathodoluminescence in Geosciences. Springer, Berlin, Heidelberg, pp 373–400

Ruthven RC, Singleton JS, Seymour NM, Gomila R, Arancibia G, Magloughlin JF, Ridley JR, Stockli DF (2019) The geometry, kinematics, and timing of deformation along the southern segment of the Paposo fault zone, Atacama fault system, northern Chile. J South Am Earth Sci 97:102355

Ryan PJ, Lawrence AL, Jenkins RA, Matthews JP, Zamora JC, Marino E, Urqueta I (1995) The Candelaria copper-gold deposit, Chile. Arizona Geol Soc Digest 20:625–645

Salazar E, Barra F, Reich M, Simon A, Leisen M, Palma G, Romero R, Rojo M (2020) Trace element geochemistry of magnetite from the Cerro Negro Norte iron oxide−apatite deposit, northern Chile. Miner Deposita 55:409–428

Sanderson DJ, Marchini WRD (1984) Transpression. J Struct Geol 6:449–458

Scheuber E, Andriessen PA (1990) The kinematic and geodynamic significance of the Atacama fault zone, northern Chile. J Struct Geol 12:243–257

Scheuber E, Gonzalez G (1999) Tectonics of the Jurassic-Early Cretaceous magmatic arc of the north Chilean Coastal Cordillera (22°–26° S): a story of crustal deformation along a convergent plate boundary. Tectonics 18:895–910

Scheuber E, Bogdanic T, Jensen A, Reutter KJ (1994) Tectonic development of the North Chilean Andes in relation to plate convergence and magmatism since the Jurassic. In: Reutter K-J, Scheuber E, Wigger P (eds) Tectonics of the Southern Central Andes. Springer, Berlin, Heidelberg, pp 121–139

Scheuber E, Hammerschmidt K, Friedrichsen H (1995) $^{40}Ar/^{39}Ar$ and Rb-Sr analyses from ductile shear zones from the Atacama fault zone, northern Chile: the age of deformation. Tectonophysics 250:61–87

Seman S, Stockli DF, McLean NM (2017) U-Pb geochronology of grossular-andradite garnet. Chem Geol 460:106–116

Seton M, Müller RD, Zahirovic S, Gaina C, Torsvik T, Shephard G, Talsma A, Gurnis M, Turner M, Maus S, Chandler M (2012) Global continental and ocean basin reconstructions since 200 Ma. Earth-Science Rev 113:212–270

Seymour NM, Singleton JS, Mavor SP, Gomila R, Stockli DF, Heuser G, Arancibia G (2020) The relationship between magmatism and deformation along the intra-arc strike-slip Atacama fault system, northern Chile. Tectonics 39:e2019TC005702

Seymour NM, Singleton JS, Gomila R, Mavor SP, Heuser G, Arancibia G, Williams S, Stockli DF (2021) Magnitude, timing, and rate of slip along the Atacama fault system, northern Chile: implications for Early Cretaceous slip partitioning and plate convergence. J Geol Soc 178:jgs2020-142

Sharman GR, Sharman JP, Sylvester Z (2018) detritalPy: a Python-based toolset for visualizing and analysing detrital geo-thermochronologic data. The Depositional Record 4:202-215

Sharp ZD (1990) A laser-based microanalytical method for the in situ determination of oxygen isotope ratios of silicates and oxides. Geochim Cosmochim Acta 54:1353–1357

Sillitoe R (2003) Iron oxide-copper-gold deposits: an Andean view. Miner Deposita 38:787–812

Simon AC, Knipping J, Reich M, Barra F, Deditius AP, Bilenker L, Childress T (2018) Kiruna-type iron oxide-apatite (IOA) and iron oxide copper-gold (IOCG) deposits form by a combination of igneous and magmatic-hydrothermal processes: evidence from the Chilean Iron Belt In: SEG 2018: Metals, Minerals, and Society, 22 - 25 September 2018, Keystone, Colorado, USA

Skirrow RG (2022) Iron oxide copper-gold (IOCG) deposits–a review (part 1): settings, mineralogy, ore geochemistry and classification. Ore Geol Rev 140:104569

Sláma J, Košler J, Condon DJ, Crowley JL, Gerdes A, Hanchar JM, Horstwood MSA, Morris GA, Nasdala L, Norberg N, Schaltegger U, Schoene B, Tubrett MN, Whitehouse MJ (2008) Plešovice zircon – a new natural reference material for U-Pb and Hf isotopic microanalysis. Chem Geol 249:1–35

Spencer CJ, Kirkland CL, Taylor RJ (2016) Strategies towards statistically robust interpretations of in situ U-Pb zircon geochronology. Geosci Front 7:581–589

Taylor BE, Liou JG (1978) The low-temperature stability of andradite in COH fluids. Am Mineral 63:378–393

Tikoff B, Greene D (1997) Stretching lineations in transpressional shear zones: an example from the Sierra Nevada Batholith, California. J Struct Geol 19:29–39

Tornos F, Velasco F, Barra F, Morata D (2010) The Tropezón Cu-Mo-(Au) deposit, northern Chile: the missing link between IOCG and porphyry copper systems? Miner Deposita 45:313–321

Tornos F, Hanchar JM, Munizaga R, Velasco F, Galindo C (2020) The role of the subducting slab and melt crystallization in the formation of magnetite-(apatite) systems, Coastal Cordillera of Chile. Miner Deposita 56:1–26

Ullrich TD, Clark AH (1998) Evolution of the Candelaria Cu-Au deposit, III Region, Chile. Geol Soc Am Abstr with Programs, p A–75

Ullrich TD, Clark AH (1999) The Candelaria copper-gold deposit, Región III, Chile: Paragenesis, geochronology and fluid composition. In: Stanley CJ et al (eds) Mineral deposits: Processes to Processing. Balkema, Rotterdam, pp 201–204

Ullrich T, Clark A, Kyser K (2001) The Candelaria Cu-Au deposit, III region, Chile: product of long-term mixing of magmatic-hydrothermal and evaporite-sourced fluids. GSA Annual Meeting, Boston, MA

Valley JW, Kitchen N, Kohn MJ, Niendorf CR, Spicuzza MJ (1995) UWG-2, a garnet standard for oxygen isotope ratios: strategies for high precision and accuracy with laser heating. Geochim Cosmochim Acta 59:5223–5231

Veloso EE, Gomila R, Cembrano J, González R, Jensen E, Arancibia G (2015) Stress fields recorded on large-scale strike-slip fault systems: effects on the tectonic evolution of crustal slivers during oblique subduction. Tectonophysics 664:244–255

Veloso E, Cembrano J, Arancibia G, Heuser G, Neira S, Siña A, Garrido I, Vermeesch P, Selby D (2017) Tectono-metallogenetic evolution of the Fe–Cu deposit of Dominga, northern Chile. Miner Deposita 52:595–620

Vermeesch P (2018) IsoplotR: a free and open toolbox for geochronology. Geosci Front 9:1479–1493

Vho A, Lanari P, Rubatto D (2020) Internally-consistent database for oxygen isotope fractionation between minerals. J Petrol 60:2101–2129

Vila T (1996) Geology of the Manto Verde copper deposit, northern Chile: a specularite rich, hydrothermal-tectonic breccia related to the Atacama fault zone. Econ Geol Spec Publ 5:157–169

Wilson J, Grocott J (1999) The emplacement of the granitic Las Tazas complex, northern Chile: the relationship between local and regional strain. J Struct Geol 21:1513–1523

Zentilli M (1974) Geological evolution and metallogenetic relationships in the Andes of northern Chile between 26 and 29 south. Dissertation, Queens University

Zheng YF (1993a) Calculation of oxygen isotope fractionation in hydroxyl-bearing silicates. Earth Planet Sci Lett 120:247–263

Zheng YF (1993b) Calculation of oxygen isotope fractionation in anhydrous silicate minerals. Geochim Cosmochim Acta 57:1079–1091